Quantum optics tools for continuous superradiant light characterization

A master's thesis presented by

Cristian Serna

at Laboratoire de Physique des Lasers (LPL)

Under the supervision of

Martin Robert-de-Saint-Vincent

Master in Physics

Erasmus Mundus Master Lascala

2026

Abstract

Novel platforms for time measurement with exceptional capabilities are of special interest as our technological limits expand, especially in the fields of communications, geolocalisation, and fundamental science. Among the new platforms, continuous superradiant lasing is one of the main options to develop novel architectures of optical clocks, with complementary strengths and trade-offs. In this thesis, the tools for characterising superradiant light are studied, designed, built, and characterised, emphasising precision and validation. Two algorithms for calculating second-order coherence ($g^{(2)}(\tau)$) were implemented and validated through simulation of laser, thermal, and pseudothermal light. Furthermore, for measuring this quantity, an experimental setup based on a single-photon detector was built and validated using a Martienssen lamp as a pseudothermal light source. In parallel, the basis for doing beat-note spectroscopy through heterodyne measurements was established, and initial tests were performed using a frequency-locked and a free-running laser. While experimental measurement of superradiant light remains for future work, this thesis paves the way for an accessible and reliable characterisation of such a light source.

Acknowledgements

During this thesis I had the opportunity to meet and work with several people, who helped to shape somehow what this final manuscript is.

I am thankful to work with my main supervisor, Martin, whose enthusiasm for science is always present and willing to contribute. I appreciate his efforts not only for scientific discussion but also other components of research and life. I would like to thank my co-supervisors, Benjamin and Bruno, who have helped and guided me during my stay in the lab.

Thanks to Yannis and Zeyuan, who have always been open to further explaining and discussing the superradiant experiment. I have understood many of the concepts and the functioning of the machine because of them.

Thanks to Fabrice for his help on the design and programming of the FPGA board, Haniffe for his work with the photodiode, Mathieu for helping me to build the light-tight box, and Romain for making several ground glass and his constant effort to make things good.

This thesis is the result of not only my work during the last six months but also my studies during the Lascala master training during the past two years. In that sense, I give the rightful thanks to Sophie Kazamias for leading such an initiative, and to the European Commission for funding it. I believe that the influence of such projects can take Europe and the world to fascinating and unexplored perspectives.

Thanks to the friends I made during the master and internship. The experience would not have been the same without you.

And finally, thanks to my family, who are always there to support me, even from afar, and to my girlfriend, Honey, for her love and support.

Contents

List of Tables

List of Figures

Nomenclature

Acronyms

AP Afterpulsing

FFT Fast Fourier Transform

FWHM Full Width at Half Maximum

HBT Hanbury-Brown-Twiss [Experiment]

PSD Power Spectral Density

PW Pairwise [method]

SC Self-convolution [method]

SNR Signal-to-Noise Ratio

SPAD Single-Photon Avalanche Diode

SWAP Sawtooth-wave adiabatic passage

Greek Symbols

Δf Linewidth / frequency variation [Hz]

Γ_R Atom transit rate [s^{-1}]

κ Photon leaking rate [s^{-1}]

ω Angular optical frequency [$\mathrm{rad} \cdot \mathrm{Hz}$]

τ Delay time [s]

τ_c Coherence time [s]

f Optical frequency [Hz]

Latin Symbols

$\hat{a}^\dagger, \hat{a}$ Photon creation and annihilation operators

$\hat{n}(t)$ Photon number operator

$\mathcal{F}$ Cavity finesse

g Single atom coupling

$g^{(2)}$ Second-order coherence

$I(f)$ Spectral intensity

L_c Cavity length [m]

N_c Atom number threshold

v Atom velocity $[\mathrm{m} \cdot \mathrm{s}^{-1}]$

v_t RGG tangential velocity $[\mathrm{m} \cdot \mathrm{s}^{-1}]$

Chapter 1

Introduction

Several sources have cited astronomy as the oldest science [1]: the study of the movement of celestial objects in the sky was the first time humanity paid careful attention to natural phenomena, trying to understand cycles and to make predictions based on them. As we talk of cycles, the concept of time emerges naturally and intrinsically linked; this way, ancient humans created calendars and were able to analyse the passage of time on a “terrestrial” scale by determining years, seasons, and days [2].

While calendars and dials based on the sun can give an approximate of moment of the year and the day, higher resolution and reliable timekeeping required new devices. That is how along history humanity has explored several physical systems to determine time: celestial trajectories, currents of water, springs, pendulums, crystal oscillators, etc, until technology developments allowed to implement the current type of systems based on atoms [2].

Atomic clocks have been implemented as frequency standards since 1955 [2], and the atomic caesium standard has been used for the official definition of the second since 1967 [3] as they can achieve a frequency stability of 10^{-16}. However, the technological improvements over the last 70 years regarding atom cooling and laser locking has allowed the fabrication of optical clocks with record uncertainties of 10^{-18} [4], and currently there is already a roadmap towards a redefinition of the second in the SI (Système international d’unités) using this type of clocks [5]. Moreover, the design and implementation of high-accuracy clocks is of vital importance for technological applications such as positioning and timing systems [6] or telecommunication networks [7], but also in fundamental science such as gravitational wave detection [8] or fundamental particle masses determination [9].

As the study of optical clocks gains relevance, a new generation of single-standard architectures has been proposed recently, as they could provide long-term stability and short-term performance. Unlike traditional systems that use atoms as a reference to lock an external laser, this new generation relies on active architectures where the clock atoms emit the laser light themselves. As part of this effort, the construction of a **continuous superradiant laser** could provide one of the necessary elements to set up such an "active" clock [10], with the potential to reduce laser sensitivity to mirror vibrations, and improve the long-term frequency stability of atomic clocks.

A fully operational, continuous-wave superradiant laser remains a significant experimental challenge worldwide, thus I joined the Magnetic Quantum Gases (GQM) group at Laboratoire de Physique des Lasers, which is about to test such device and in this master's thesis I aim to take part in the operation and characterisation of the system.

1.1 Aim

The aim of this thesis is to design, build and characterise the necessary tools for characterisation of continuous superradiant light, as it is of particular interest for analysing the evolution of the system and to confirm the emission of superradiant light from the laser prototype. Particularly, the focus is to set up two characterisation methods:

- **Second-order coherence measurement**, to study temporal correlations, of importance for analysing intensity fluctuations that can affect measurement noise on a clock, and to analyse the quantum statistical nature of the light source;

- **Beat-note spectroscopy**, to determine the exact frequency of the output light, its linewidth, and as it could be used later on for locking other laser sources or beat with a frequency comb for being used as optical clock.

Additionally, since the characterisation is part of the wider superradiant project, a brief review of the motivation and status of the laser prototype is given.

1.2 Delimitations

As of July 6th 2026, the superradiant prototype laser has not achieved superradiance yet. The key bottlenecks are identified, particularly, velocity spread control by laser cooling, and efforts to overcome them are ongoing. As there is no superradiance, the characterisation methods cannot be used yet in the system; however, in the present master's thesis we test them thoroughly by other means to ensure their correct implementation and their reliability to properly characterise the output superradiant light.

1.3 Thesis outline

This thesis is divided into 4 chapters:

Chapter 2 gives a brief description of the current state of the project of the superradiant laser, including a glimpse of optical clocks and superradiance theory, the methods and why doing a quantum characterisation of the outgoing light from the machine is necessary.

Chapter 3 is dedicated to the description of second-order coherence $g^{(2)}(\tau)$, the setup and methods implemented for its determination, and the results of both simulations and experiments regarding this technique.

Chapter 4 is focused on the details of heterodyne detection, its implementation and the results from experimental measurements of 2 reference beams, showing its potential use for characterising other light sources.

Chapter 5 presents the conclusions of this work based on the results and prospects for its continuation as part of a PhD thesis.

Chapter 2

Superradiance and clocks

One of the current projects of the Magnetic Quantum Gases (Gaz Quantiques Magnétiques in French, GQM) at the Laser Physics Laboratory (Laboratoire de Physique des Lasers in French, LPL) has as objective to build one of the first continuous superradiant lasers. The long-run purpose is to investigate the collective emission dynamics of the ensemble of atoms and assess the performance of this architecture as one of the first continuous active optical clocks [1]. In the subsequent sections, I outline the theoretical framework of superradiance, indicate the main differences between current designs of optical clocks and this proposal, and describe the current status of the experimental project.

2.1 Superradiant lasing

Superradiance is a phenomenon in which an ensemble of atoms (or molecules) emits light spontaneously and coherently. A key difference between superradiance and stimulated emission is that the coherence of the system is not stored within an electromagnetic field mode—as is the case of lasers with an optical cavity—but in the ensemble itself. This coherence manifests itself as a macroscopic, collective atomic dipole that remains highly robust against fluctuations

[1] Although it could be the first continuous Active Optical Clock with a narrow transition (see [11] for an AOC based on Cs)

as a result of atomic self-synchronization.

This phenomenon has been observed since the 1970s [12]; however, it gained renewed importance over the last two decades. Advancements in laser cooling techniques enabled the successful detection of steady-state superradiance, showing for the first time experimentally the properties of a superradiant high-spectral purity laser [13], although without achieving continuous operation.

This new type of lasers is said to operate on the superradiant regime, also called "bad-cavity regime". In this regime, the linewidth of the cavity mode is much wider than the linewidth of the gain profile of the medium (atomic transition linewidth); meaning that the decay rate of the atoms is much lower than the losses of the cavity, so very few intra-cavity photons remain compared to the case of conventional lasers [14, 15].

Using the superradiant regime comes from the linewidth requirements for an optical clock: a narrow linewidth can be achieved by using an atomic transition (narrower than the cavity linewidth). However, this setup implies a low spontaneous emission rate, with very low output intensity I coming from fluorescence. As the medium does not provide significant stimulated emission gain due to the low intra-cavity photon number, superradiance is an interesting phenomenon due to its emission enhancement [13, 14]. Moreover, superradiance does not strictly require a cavity, but the cavity mode field contributes to build up the coherence of the ensemble and define an emission mode, making it a necessary element for experimental and practical applications [16].

Despite the progress achieved on superradiant lasers, the current state-of-the-art machines can only generate up to 0.1 s pulses due to their working principle: an ensemble of excited atoms inside a cavity de-excites by emitting light; to have a new emission it is necessary to either replace the de-excited atoms with another ensemble of excited atoms, or re-excite the atoms inside the cavity with an external beam, which disadvantageously can also heat up the ensemble, kicking atoms out of the cavity and stopping the lasing [17, 18, 19]. Although this process is imperfect, it has been enough to show that steady-state superradiance can be achieved.

Naturally, the next development step is to achieve continuous superradiant lasing, with one of the simplest techniques for this relying on a hot atomic beam excited just before the atoms reach the cavity mode, where they could emit in a superradiant fashion if the conditions are adequate [20]. Such simplicity would allow easy and cost-effective reproducibility, and even field deployment for out-of-the-lab applications.

2.2 Microwave and Optical Atomic Clocks

As previously mentioned, the current technologies used for time keeping are based on atomic systems. These exploit the fact that atomic transitions are, in principle and under the same conditions, dependent only on the atomic species. This way two atoms of the same isotopic species would have the same energy level structure. These energy transitions can then be related to photon energy, and therefore to a frequency that can be used to count time.

The current standard is based on the hyperfine levels of caesium-133, which are selected and excited by microwaves. The excitation of the atoms is done using a Ramsey sequence in two $\pi/2$-pulses, and then the final state is probed by atomic fluorescence corresponding to the transition from one of the hyperfine levels to an upper energy level. The resulting light is measured by a photodiode and the signal is used to tune the exciting microwave [21], which is then used in an "electronics package" able to process and measure the signal directly, detecting a frequency ticking that may be used to define time [22].

When defining a frequency reference, a standard figure of merit is its stability, i.e, how much the signal from the standard fluctuates over time. For a given clock, it is possible to determine the achievable instability determined by the Allan deviation over an integration time τ according to [23]:

$$\sigma_y(\tau) = \frac{1}{K}\frac{1}{Q}\frac{1}{SNR}\sqrt{\frac{T_c}{\tau}}, \tag{2.1}$$

with SNR the signal to noise ratio, $Q = \frac{f}{\Delta f}$ the quality factor coming from the radiation linewidth Δf and the absolute frequency f, T_c the total cycle time (atom preparation and interrogation time), and K a factor of order 10^0 given by:

$$K = \frac{dI(f)}{df}\frac{\Delta f}{I_{max}},$$

where $I(f)$ is the signal intensity.

The latest caesium fountain clocks have achieved an Allan deviation down to $1.5 \times 10^{-13}\,\tau^{-1/2}$, corresponding to a statistical uncertainty of 3.5×10^{-16} over 20 days of measurement time [24]. Although this limit means having an uncertainty of just a few hundreds of picoseconds per day, it can be easily improved conceptually according to equation (2.1) by increasing the quality factor, i.e., using narrower linewidths or higher absolute frequencies. This is the case of optical clocks: several experiments[2] have already achieved lower instability than caesium clocks by using radiation in the hundreds of THz frequency, corresponding to visible light, while maintaining narrow linewidth exploiting forbidden atomic transitions.

As in the case of caesium clocks, optical clocks take advantage of a narrow atomic transition to tune the frequency of an external radiation source (laser). This procedure has several issues regarding frequency stability: as lasers are used to probe and excite the atoms, besides acting as clock light source, their own stability affects the clock stability in the long term according to the Dick effect [28]. Even more, as the driving laser requires working in the good-cavity regime, its stability is limited by the thermal fluctuations of the cavity, increasing further the uncertainty of the clock light.

To solve these issues, active optical clocks have been proposed [15], and several research groups are working on them currently[3]. In this architecture, clock light is emitted directly by the atoms in the bad-cavity regime. This connects directly with our previous discussion on superradiant lasers: a novel "active" optical clock based on continuous superradiant lasing has the potential to improve long-term frequency stability and provide short-term performance.

[2] See for example [25], [26], [27]

[3] Reference [29] has an extensive list of groups working on bad-cavity superradiant lasers with details on the used architecture and achievements

2.3 Experimental setup at LPL

At LPL, a prototype for a superradiant laser has been built. The prototype, based on the proposal presented in [20], is part of the Strontium 2 (or superradiance) project. The experimental setup follows this sequence: Strontium (Sr) atoms are sublimed from Sr metal chunks inside an oven, then the atoms exit in a wide direction through microtubes, and after exiting they are transversally cooled (by laser cooling techniques) to reduce their dispersion and move towards a Zeeman slower.

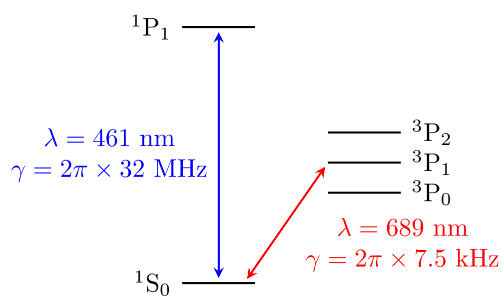

Figure 2.1: **Transition diagram of ^{88}Sr**. The 461 nm line is used for Zeeman and transversal cooling, as well as for measuring the population of the $^1S_0$ level through fluorescence. The 689 nm line is used for atom excitation and SWAP cooling. It is also the one on which superradiant emission is searched.

At the exit of the Zeeman slower, the atoms enter the science chamber shown in Figure 2.2 through an opening on the right side. Inside the chamber, the atoms are deflected towards an optical high-finesse cavity using radiation pressure, exerted by a laser beam (coming from the lower part of the image; not shown), and further transversally cooled in 2 stages before reaching the cavity. Once they enter the cavity, the atoms are excited before the cavity mode following a scheme of adiabatic transition that guarantees population inversion. Finally, once they reach the cavity mode, they may emit in a superradiant fashion, or they may also be probed by fluorescence to check the correct functioning of the steps of the setup by analysing total number of excited atoms.

The experiment is done using the ^{88}Sr isotope. The energy transitions used along with their corresponding wavelength and linewidth are shown in Figure 2.1. The initial transversal

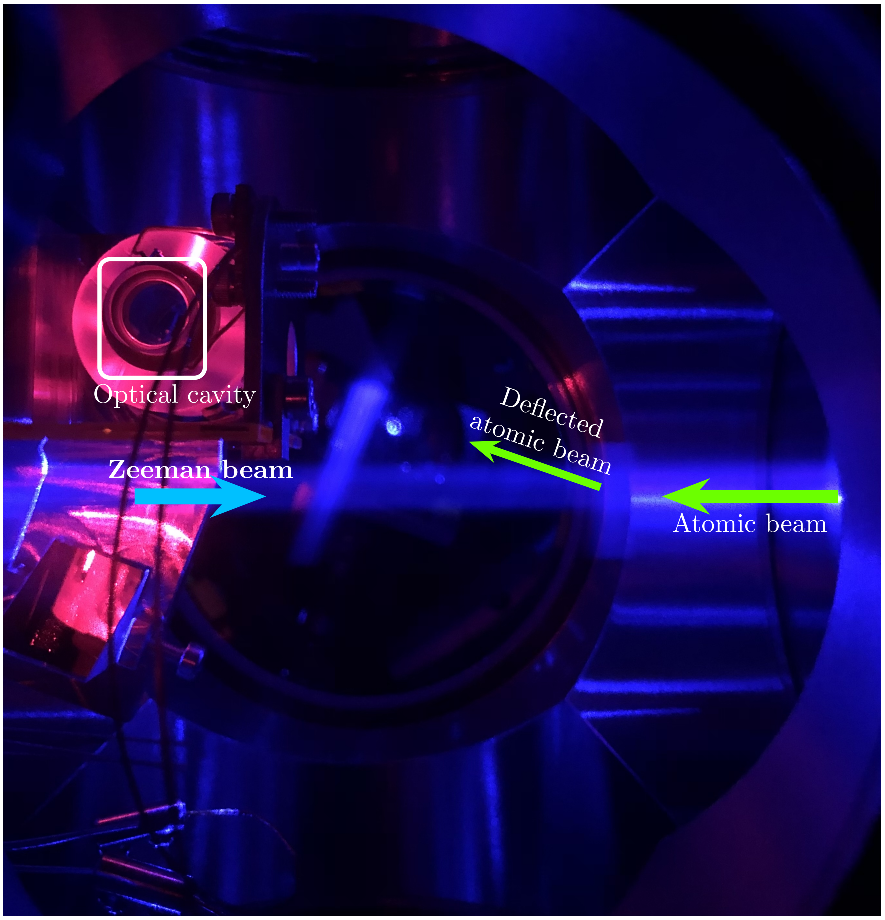

Figure 2.2: **Science chamber of the Superradiance experiment** to build a continuous superradiant laser. The atoms come into the chamber from the right after a Zeeman slower. Inside the chamber they are deflected towards the optical cavity and transversally cooled using laser beams (not shown in the image). *Credits original picture: Yannis Pargoire*

cooling and the Zeeman cooling are done using the $^1S_0 \leftrightarrow ^1P_1$ transition corresponding to a 461 nm laser, which is locked on the atoms using Modulation Transfer Spectroscopy (MTS). The deflection and the first stage of the posterior transverse cooling uses the same transition, but for the second stage, sawtooth-wave adiabatic passage (SWAP) cooling[4] is used on the $^1S_0 \leftrightarrow ^3P_1$ transition with a 689 nm laser. This transition is also used for the atomic excitation and corresponds to the possible superradiant emission. Moreover, to determine the number of atoms in the cavity and the population inversion, fluorescence of the 461 nm beam is used to

[4]SWAP cooling is a recently developed laser cooling technique suitable for narrow transitions where cycles of spontaneous and stimulated emission are used, resulting in cooling by radiation pressure [30].

probe the atoms with and without previous excitation.

Table 2.1: **Experimental and expected parameters of the experiment.**

Parameter	**Value**
Cavity length, L_c	22.61 ± 0.2 mm
Cavity finesse, $\mathcal{F}$ (in vacuum)	8900 ± 400
Photon leaking rate, κ	$2\pi(630 \pm 15)$ kHz
Atom velocity, v	10–100 m/s
Atom transit rate, Γ_R	2π(23.5–235) kHz
Atom number threshold, N_c	17–80

In this architecture, continuous superradiant lasing is achieved by an atomic ensemble that renews its excited atoms by a constant flux, where an atom in excited state reaches the ensemble, couples to the collective atomic dipole, and then emits light. As the incoming atoms continue travelling forward, they leave the cavity mode short after entering, whether they emit light or not [31]. As has been previously studied in the research team [31, 32], a fundamental threshold condition for superradiant lasing is given by

$$N > N_c = \frac{\Gamma_R \kappa}{2g^2},$$

where Γ_R is the atom transit rate, κ is the cavity leaking rate, and g is the single atom coupling given by [16]:

$$g = -\frac{\hat{\epsilon} \cdot \vec{d}}{\hbar} \sqrt{\frac{\omega}{2\epsilon_0 \hbar V}}, \tag{2.2}$$

with $\hat{\epsilon}$ the polarization of the cavity field, $\vec{d}$ the dipole matrix element of the atomic transition, V the volume of the cavity mode, ω the frequency of the light and ϵ_0 the vacuum permittivity.

Following this condition, and considering the parameters of the experiment shown in table 2.1, the atom number threshold in the cavity mode to observe superradiance is between 17 and 80, depending on the range of velocities of the atoms that reach the cavity. However, this latter condition is sufficient only if the Doppler width introduced by the velocity of the atoms in the cavity axis (the axial velocity) is small [20], with both conditions relating to the synchronisation rate of the dipoles when they enter the cavity. In short, superradiant emission in the setup requires a determined number of atoms and low axial velocities. Although the first condition has been achieved and confirmed experimentally, further improvement on SWAP cooling or even higher atomic flux are necessary to observe superradiance.

The light that exits the cavity can be studied in the time domain or in the frequency domain, as in [33]. An analysis on the time domain with high temporal resolution by using a Single Photon Avalanche Photodiode (SPAD) and an associated counting and time tagging module would allow one to study the temporal evolution of the light intensity. It would also make possible to determine the second-order coherence and analyse temporal correlations and changes of superradiance regime. On the other hand, studying the light on the frequency domain enables to precisely determine the emitted frequency and linewidth, providing information on the atomic transition and the mechanism leading to it, respectively.

Chapter 3

Time-domain characterisation

Most conventional light sources produce chaotic light because the phenomena linked to its generation come from emission of large groups of atoms, each one emitting with random phases and frequencies. However, if there are other mechanisms or elements at play (stimulated emission, superradiance, collimation optics, etc), light might have phase and intensity correlations to some extent yielding interesting effects as a consequence [34].

In classical optics, coherence and correlation are standard quantities used to characterise the nature of light; for instance, they determine the visibility in interferometric setups, enabling applications using temporal and spatial coherence such as optical coherence tomography (OCT), coherent anti-Stokes Raman Scattering (CARS), and ultrafast spectroscopy. In quantum optics, a standard approach is to exploit temporal coherence through the determination of first-, second-, or higher-order coherence, to discern the nature of light (quantum or classical) [35].

A full characterisation of quantum optical coherence requires the determination of all the higher-order coherence functions. This can be achieved by photon coincidence counts, with the nth-order needing n simultaneous detections [36]. This approach is cumbersome as it would not only require n detectors with their corresponding electronics and time-tagging hardware, but also incredible computational power as the complexity scales as the n-th power of the total number of detections per detector N ($O(N^n)$). In the context of this thesis, the determination of second-order coherence is enough to establish the quantum nature of light and to investigate quantum correlations, as will be discussed in the next sections.

3.1 First and second-order coherence

Before the theories on quantum theory of optical coherence that were born during the 1950s due to the photon counting experiments, temporal coherence had been defined using just the autocorrelation of the electric field E as a function of time delay [34]:

$$G(\tau) = \langle E^*(t)E(t+\tau)\rangle_t, \tag{3.1}$$

with $\langle\,\rangle_t$ denoting the time average; the t is removed from now on to ease the notation. Note that the average field intensity $I(t) = \langle|E(t)|^2\rangle$ is obtained for $\tau = 0$. From this quantity, the degree of temporal coherence is defined as the normalized autocorrelation [34]:

$$g(\tau) = \frac{\langle E^*(t)E(t+\tau)\rangle}{\langle E^*(t)E(t)\rangle}, \tag{3.2}$$

which measures the electric field degree of correlation. For a perfectly monochromatic plane wave, $|g(\tau)| = 1$ always, which means that the electric field remains correlated.

3.1.1 Definition

In quantum field theory, the electric field (now acting as an operator $\mathbf{E}(t)$) can be separated in creation $\mathbf{E}^{(-)}$ and annihilation $\mathbf{E}^{(+)}$ operators such that $\mathbf{E}(t) = \mathbf{E}^{(+)}(t) + \mathbf{E}^{(-)}(t)$. In the detection process of a light field, photoionization detectors[1] absorb photons, corresponding only to the action of the annihilation operator [37]. Next, assuming for simplicity the field is linearly polarized, replacing this operator in Equation 3.2 and taking the complex conjugate

[1]As are single photon detectors.

as the Hermitian conjugate yields:

$$g^{(1)}(\tau) = \frac{\langle E^{(-)}(t)E^{(+)}(t+\tau)\rangle}{\langle E^{(-)}(t)E^{(+)}(t)\rangle}, \tag{3.3}$$

usually called first-order coherence function. This function can be seen as a measure of the degree of coherence of the electric field amplitude of an electromagnetic wave at different propagation times, and its non-normalised version can be used to predict the detection rate of an ideal photodetector [36]. Now, defining in a similar manner the two-photon coincidence rate by considering a photon absorption at time t followed by the next photon at time $t+\tau$ [37]:

$$g^{(2)}(\tau) = \frac{\langle E^{(-)}(t)E^{(-)}(t+\tau)E^{(+)}(t+\tau)E^{(+)}(t)\rangle}{\langle E^{(-)}(t)E^{(+)}(t)\rangle^2}.$$

Now, if we use the radiation intensity definition $I(t) = E^{(-)}(t)E^{(+)}(t)$, this last equation can be written in the form:

$$\boxed{g^{(2)}(\tau) = \frac{\langle : I(t)I(t+\tau) : \rangle}{\langle I(t)\rangle^2}} \tag{3.4}$$

with :: indicating normal ordering[2]. Following the same interpretation as for the first-order of coherence, this equation represents the degree of coherence of the intensity at time delay τ.

For single-mode light, the intensity is given in terms of annihilation and creation operators as $I(t) \simeq \mathcal{E}^2 a^\dagger a = \mathcal{E}^2 \hat{n}(t)$ with $\mathcal{E}$ related to the amplitude of the electric field per photon in the mode, and $\hat{n}$ the number operator. Replacing this definition of the intensity in Equation 3.4 with a time delay $\tau = 0$ produces the following:

$$g^{(2)}(0) = \frac{\langle n(n-1)\rangle}{\langle n\rangle^2}, \tag{3.5}$$

with n the number of photons in the mode at time delay zero. Note that for large photon numbers the approximation $n(n-1) \approx n^2$ may be applied, which is equivalent to dropping

[2]Normal ordering indicates that all creation operators go before annihilation operators. Note that the commuting property of $E^{(+)}$ operators is used.

the normal ordering. Doing this approximation for the general case $\tau \neq 0$ yields:

$$\boxed{g^{(2)}(\tau) = \frac{\langle n(t)n(t+\tau)\rangle}{\langle n(t)\rangle^2}.} \tag{3.6}$$

Let us focus now on the interpretation of these quantities and their values for different types of source of light.

3.1.2 Light sources classification

There are several interpretations of $g^{(2)}(\tau)$, the most common of which relates to the temporal distribution of photons. Figure 3.1 illustrates three general cases: bunched, random, and antibunched light. Consider a detector receiving photons from each of these source types: bunched photons tend to arrive in close clusters, random photons are distributed over time with no particular pattern in their arrival times, and antibunched photons tend to arrive well-separated from one another. These behaviours correspond to $g^{(2)}(\tau)$ values greater than one, equal to one, and less than one, respectively [38].

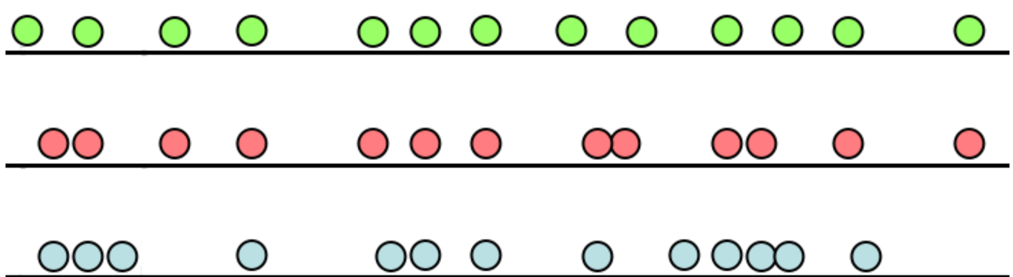

Figure 3.1: (Green) **Antibunched,** (red) **random, and** (blue) **bunched light representation.** Each circle represents a photon arrival to a detector over time (horizontal axis). Image adapted from [39].

This interpretation has a direct connection with physical sources of light: $g^{(2)}(0)$ is typically used to identify **nonclassical light**, i.e. quantum light, as values below unity are impossible at $\tau = 0$ for classical sources of light. Furthermore, the specific lower bound of $g^{(2)}(\tau)$ can

Table 3.1: **Interpretation of the value of $\mathbf{g^{(2)}(0)}$** by type of physical system, temporal behaviour and type of statistical distribution.

$g^{(2)}(0)$	**Physical system**	**Temporal behaviour**	**Statistical distribution**
< 1	Quantum states	Antibunching	sub-Poissonian
$= 1$	Coherent light	Random	Poissonian
> 1	Chaotic light	Bunching	super-Poissonian

help to determine if a source of light acts as a single-photon emitter. On the classical side, **coherent states**[3], as the light emitted by a laser above threshold, yield a constant $g^{(2)}(\tau)$ of one. Finally, **chaotic light**, such as that generated by thermal radiation, follows $g^{(2)}(0) = 2$, meaning the probability of detecting coincident photons is greater than in the coherent case [38]. Moreover, an interpretation of $g^{(2)}(\tau)$ based on the photon statistics is also common, with the corresponding distribution as shown in table 3.1. As in the classical interpretation of optical coherence, light fluctuations stop being correlated over long times, such that for a steady-state source, the arrival times are random and the source behaves as a coherent light source:

$$g^{(2)}(\tau) \to 1, \quad \tau >> \tau_c,$$

with τ_c known as the coherence time, and usually defined as the value at which $g^{(1)}(\tau)$ drops to an established value, usually $1/e$ or based on the half-width at half-maximum [34].

3.2 Determination methods

As seen in the previous section, $g^{(2)}(\tau)$ can be calculated from equations 3.4 and 3.6, however, experimental measurements and computational processing are done by taking discrete times. In this section, we show two techniques used for its calculation.

[3]Coherent states are quantum states; however, they are the closest representation of a classical field in quantum mechanics.

3.2.1 Full pairwise cross-correlation or histogram method

Consider Equation 3.6, writing the integral form of the numerator produces:

$$\langle n(t)n(t+\tau)\rangle = \frac{1}{T}\int_0^T n(t)n(t+\tau)dt,$$

with $T >> \tau_c$ the total experiment time and the coherence time, respectively. Discretising this expression so it can be computationally calculated results on:

$$\langle n(t)n(t+\tau)\rangle = \frac{\Delta t}{T}\sum_i n(t_i)n(t_i+\tau),$$

where time has been discretised in equal time bins Δt, and $n(t_i)$ representing the number of photons detected in a bin centered on t_i. Note that the term of the summation is not null only when there are photons detected at separation τ. Calculating this summation is then equivalent to building the histogram of the number of counts per time bin as function of time delay τ, thus the method is called **histogram method**, or also, **full pairwise cross-correlation method** (PW method, in short) for reasons that will become clear later.

Continuing with Equation 3.6, the previous process misses a normalisation factor:

$$\langle n(t)\rangle^2 = \left[\frac{1}{T}\int_0^T n(t)dt\right]^2,$$

discretising once again:

$$\langle n(t)\rangle^2 = \left(\frac{\Delta t}{T}\right)^2\left(\sum_i n(t_i)\right)^2,$$

with the term of the summation being the number of photons at each time t_i, thus it is equivalent to the total number of photons N. Joining the results:

$$g^{(2)}(\tau) = \frac{\frac{1}{T}\sum_i n(t_i)n(t_i+\tau)}{N^2\frac{\Delta t}{T^2}}, \tag{3.7}$$

where the numerator is then counts per second, and the denominator is the corresponding normalisation factor for 1 detector detection.

Before introducing the specific steps of the method, let us consider the typical experimental setup used for $g^{(2)}(\tau)$ determination: the Hanbury-Brown-Twiss (HBT) experiment, shown in Figure 3.2. In this setup, a photon stream to be sampled is directed towards a balanced beamsplitter, with each one of the outputs coupled to different single-photon detectors, which are then connected to a time-tagging device.

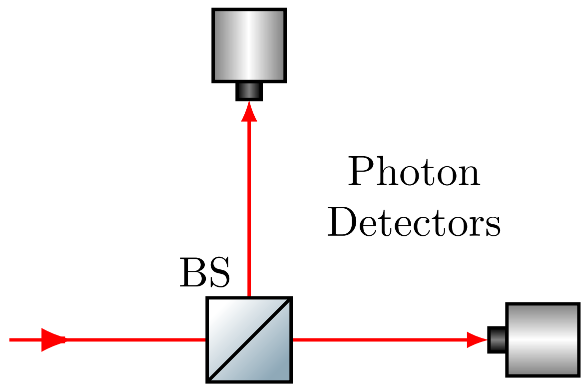

Figure 3.2: **Hanbury-Brown-Twiss experimental setup.** BS is a 50:50 beamsplitter.

The HBT setup has several advantages regarding photon detection: it makes possible to detect two photon arrivals temporally close if they are split by the beamsplitter, therefore $g^{(2)}(\tau)$ could be determined for small time delays (including $\tau = 0$)[4].

Now, with the collected data (the photon time arrivals in each of the detectors) the histogram method requires the following steps[5]:

1. Calculate the time delays τ between each pair of photons from different detectors as shown in Figure 3.3.

2. Build a histogram of the number of counts per time delay bin $\Delta\tau$. Each time bin corresponding to a range of possible time delays such that $\Delta\tau < \tau_c$ so the decoherence effects are observable.

[4]Currently, there are single-photon arrays which can detect multiple arrivals over a surface; although their capabilities enable to calculate $g^{(2)}(\tau)$ even at $\tau = 0$ [35], there might be scenarios where an HBT setup provides more information on the system, at the same time that is more cost-effective.

[5]This description is based on the implementation of the method found in [40]

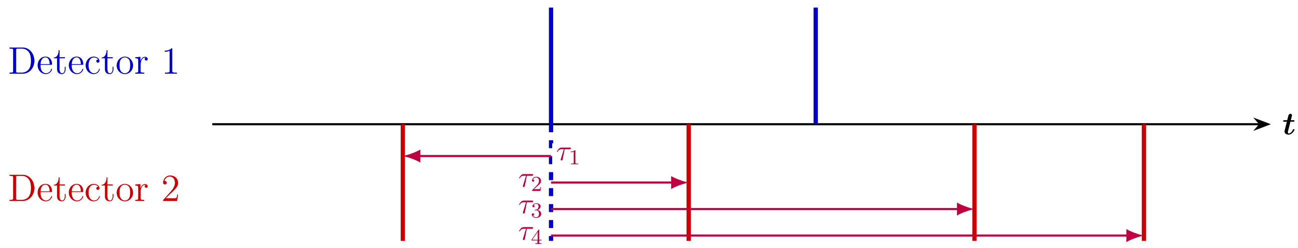

Figure 3.3: **Time delays determination process for histogram method.** The first detection done by one of the detectors is picked, then the time difference to the other detections from the second detector is determined, finally the resulting time delays τ_1 to τ_4 are saved for later determination of $g^{(2)}(\tau)$. The same process is repeated for every arrival at the detector 1.

3. Calculate $g^{(2)}(\tau)$ by normalising the counts per second with respect to the total number of expected counts per time delay bin per second.

In this case, the total number of expected counts per delay bin per second is given by:

$$E_2 = \frac{N_1 N_2}{T^2} \Delta\tau, \tag{3.8}$$

with N_1 and N_2 the total number of detections in each detector and T the total time span from the first photon to the last one.

As far as has been shown, this calculation process does not require two detectors: the only reason why two detectors and a beamsplitter are used is to overcome the detection limitations of these devices. Therefore, it is valid to ask: what if we had a detector able to detect simultaneous photons on its own?

This topic is worth discussing and is covered in section 3.4, where an experimental setup based on only one detector is shown. Meanwhile, following the same steps as before, it is possible to determine $g^{(2)}(\tau)$, with the only difference being that the time delays are determined by comparing each arrival in one detector with the other arrivals.

3.2.2 Self-convolution method

Calculating all the possible time delays is a computationally intensive task with complexity $O(N_1 \times N_2)$. Under that consideration, some authors have proposed alternative methods to estimate the second-order coherence that would make the task faster [41].

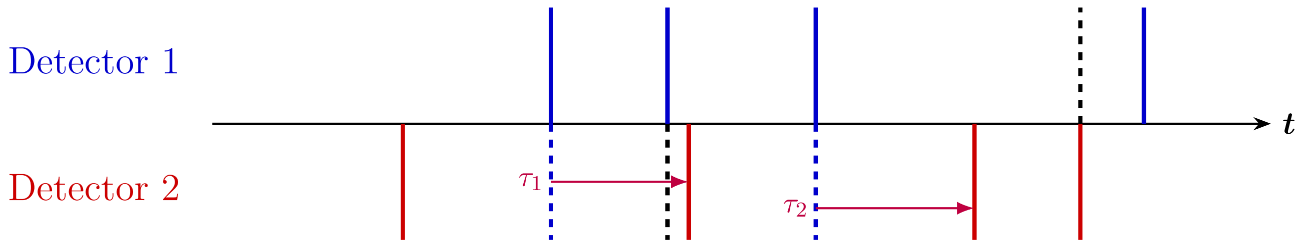

Figure 3.4: **Start-stop scheme for self-convolution method.** In this configuration, time delays are calculated only between ordered times of different detectors. An arrival on detector 1 sets the "start" time, which is finished by an arrival on detector 2 ("stop"); any arrival between both detections on detector 1 is ignored, as well as arrivals on detector 2 without a previous arrival on detector 1. The dashed black lines indicate ignored arrival times.

In this method, $g^{(2)}(\tau)$ can be estimated from [41]:

$$g^{(2)}(\tau) = \frac{J(\tau)}{\bar{I}}, \tag{3.9}$$

with $\bar{I}$ the average photon detection rate, and $J(\tau)$ is defined as follows: consider an HBT setup (Figure 3.2); as before, the time delays of the photon arrivals are also calculated, but following a different scheme, as shown in Figure 3.4. Now consider a detection at time $t = 0$, the probability of detecting the m-th next photon at time τ is given by $L_m(\tau)$.

$J(\tau)$ is then defined as [42]:

$$J(\tau) = \sum_{m=1}^{\infty} L_m(\tau). \tag{3.10}$$

To be able to estimate $J(\tau)$ from the time delays in the start-stop scheme, consider $K(\tau)$ as the probability of detecting the next photon at time τ. This function follows [42]:

$$\int_0^{\tau} K(\tau')L_m(\tau - \tau')d\tau' = L_{m+1}(\tau);$$

and therefore $J(\tau)$ can be calculated as the series of self-convolutions of $K(\tau)$:

$$J(\tau) = \sum_{n=0}^{\infty} K_n(\tau), \tag{3.11}$$

with $K_n(\tau)$ the n-th self-convolution of $K(\tau)$: $K_n(\tau) = K_{n-1}(\tau) * K(\tau)$, with $*$ the convolution operator, hence the name of the method: **self-convolution method** (SC method, in short).

Finally, note $K(\tau)$ can be estimated from the start-stop scheme by building the normalised histogram of the measured time delays. Further details on the implementation of the method in the HBT experiment can be found in [41], however, let us focus on the single detector scheme. In that case, the start-stop scheme can be implemented by just calculating the time delays as the time difference between each consecutive pair of detections as shown in Figure 3.5.

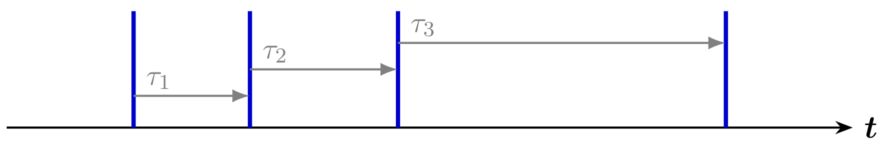

Figure 3.5: **Start-stop scheme for self-convolution method with one detector.** The time delay is calculated for every pair of consecutive arrivals.

3.3 Methods implementation and validation

The previous methods were implemented computationally using Python. The implementation of the histogram method was based on the code found in [40], for which the delays were calculated considering the list of times of just one detector. In addition, the logic was vectorised to improve computational efficiency. For the self-convolution method, an implementation using fftconvolve was done, however, inconsistent results were found as will be shown in the next subsections.

Several computational parameters were considered for both implementations: a maximum time delay and maximum number of samples are set by the user because computing over all the collected data is computationally heavy and not always necessary; time delay bin width is also to be set depending on the dataset to analyse.

Another parameter to set in the case of the self-convolution method is the maximum convolution order M, corresponding to the maximum $K_M(\tau)$ to include in Equation 3.11. To choose M, several recommendations are given in [41], but only in the case where the light to be analysed is chaotic. This way, for chaotic light the basic requirement to follow to achieve convergence and low error is:

$$\bar{I}\tau_c << 1, \tag{3.12}$$

with error $(0.8\bar{I}\tau_c)^M$. No criterion is given for other types of light sources.

As the methods are implemented, a validation of their proper functioning becomes necessary. Therefore, Monte-Carlo simulations of different light sources were implemented and the corresponding $g^{(2)}(\tau)$ calculated based on generated lists of detection times. In general, the simulations are based on this process:

1. Generate the temporal intensity profile of the light source to simulate.

2. Scale the intensity according to the desired mean photon detection rate.

3. Do Poisson sampling of the intensity: The expected number of events is set as the intensity times the temporal binning, and the actual number of events is a random number following the Poisson distribution with such expectation value.

4. Calculate $g^{(2)}(\tau)$ using the calculation methods.

5. Average $g^{(2)}(\tau)$ over several simulations.

In the next subsections, I discuss how to obtain the temporal intensity profile for each analysed light source.

3.3.1 Laser light

Laser light has two relevant characteristics for being used as a validation method: first, the counts distribution is known to be Poissonian, and second, it implies $g^{(2)}(\tau) = 1$ for all τ. Therefore, a simulation of this type of source can be checked statistically, and the proper normalisation of the implemented methods can be verified.

Considering an ideal laser, the output intensity profile is $I(t) = A$, with A an arbitrary constant. The relevant parameter to be set up in the simulation is given by the mean photon rate (MPR) $\mathcal{R}$, while for the second-order coherence determination, the relevant parameter is only the bin width, with no interest in total simulation time as an ideal laser follows $\tau_c \to \infty$.

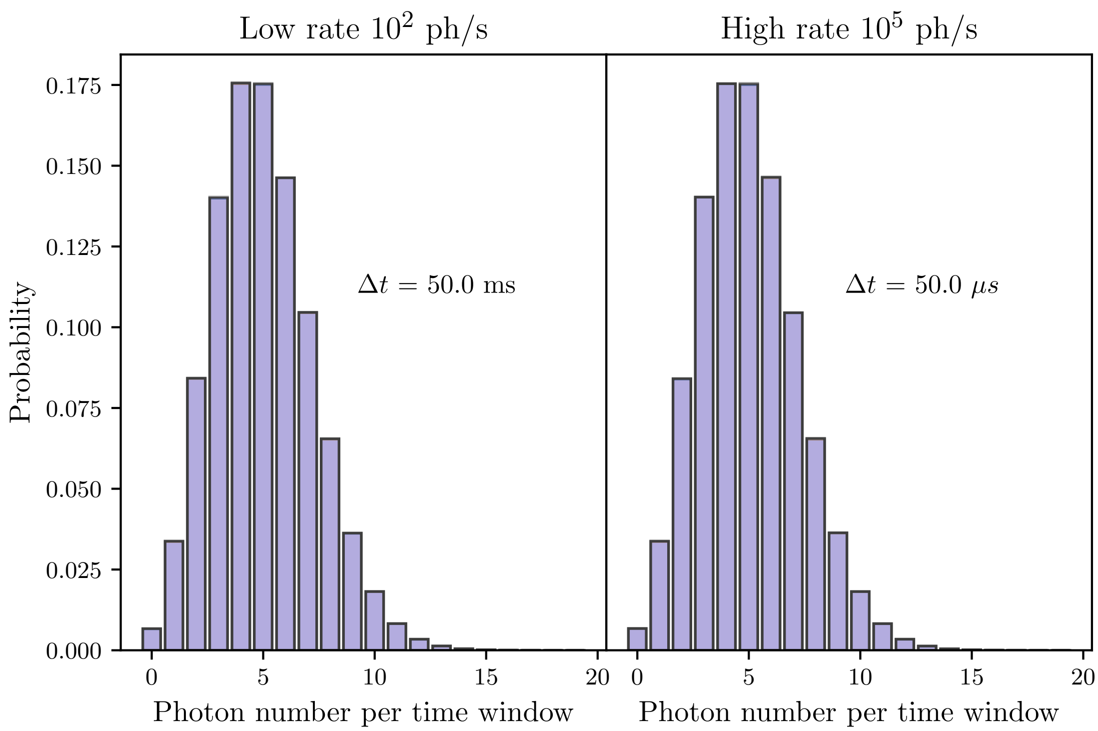

Figure 3.6: **Photon number distribution per time window for simulated laser sources.** Low rate (10^2 ph/s) and high rate (10^5 ph/s) simulations are shown with their corresponding time window to achieve a mean value of 5 photons per time window. The average of the data and the average corresponding Poissonian Probability Mass Function (PMF) overlap almost perfectly.

To analyse the relevant parameters, two types of datasets were simulated: one at high photon rate (10^5 photons per second, or ph/s) and the other at low photon rate (10^2 ph/s). Each simulation type was run 150 times with a total number of photon of approximately 10^5 to calculate the corresponding photon number distribution and second-order coherence for each realisation.

The average photon number distributions for both simulation types are shown in Figure 3.6. For each run, the time window Δt was defined as $\Delta t = n_{exp}/\langle \mathcal{R} \rangle$, where $n_{exp} = 5$ represents the expected number of photons per window. The obtained average time windows were found to be in agreement with the set mean rate.

Furthermore, a theoretical Poissonian Probability Mass Function (PMF) with argument $\mathcal{R} \times \Delta t$ was calculated for each run. The resulting average of the PMFs corresponds with the experimental data in Figure 3.6. As the data distribution follows the PMF, the Poissonian distribution of the simulations is confirmed.

Two different binning widths were chosen to analyse their impact on the $g^{(2)}(\tau)$ retrieval, taking into account the simulated photon rates and experimental restrictions. Regarding the first binning $\Delta\tau = 100$ ns, it is easily achievable by commercial detectors and related processing modules. Moreover, it is well below the average waiting time (the average time between two consecutive photons), corresponding to $\mathcal{R}^{-1} = 10$ ms and $10\,\mu$s for each respective rate. For the second binning $\Delta\tau = 10\,\mu$s, it is still below one of the rates, but matches the inverse of the rate of one of the simulations, which yields undesirable results as will be shown.

In the case of self-convolution, a high convolution order was chosen (100 or 1000, depending on the dataset) as the calculation time was still short for high convolution order.

The resulting $g^{(2)}(\tau)$ are shown in Figure 3.7. Each plot shows the resulting $g^{(2)}(\tau)$ for the 150 runs in light color, and their corresponding average in darker color. In general, $g^{(2)}(\tau) \approx 1$ along all the analysed time delays using the PW method. This matches the expected result for a Poissonian source. On the other hand, for the low-photon rate simulations, the SC method yields identical results, with the same average and dispersion. However, for high photon rate, the result is slightly higher than 1 and has lower dispersion when narrow binning

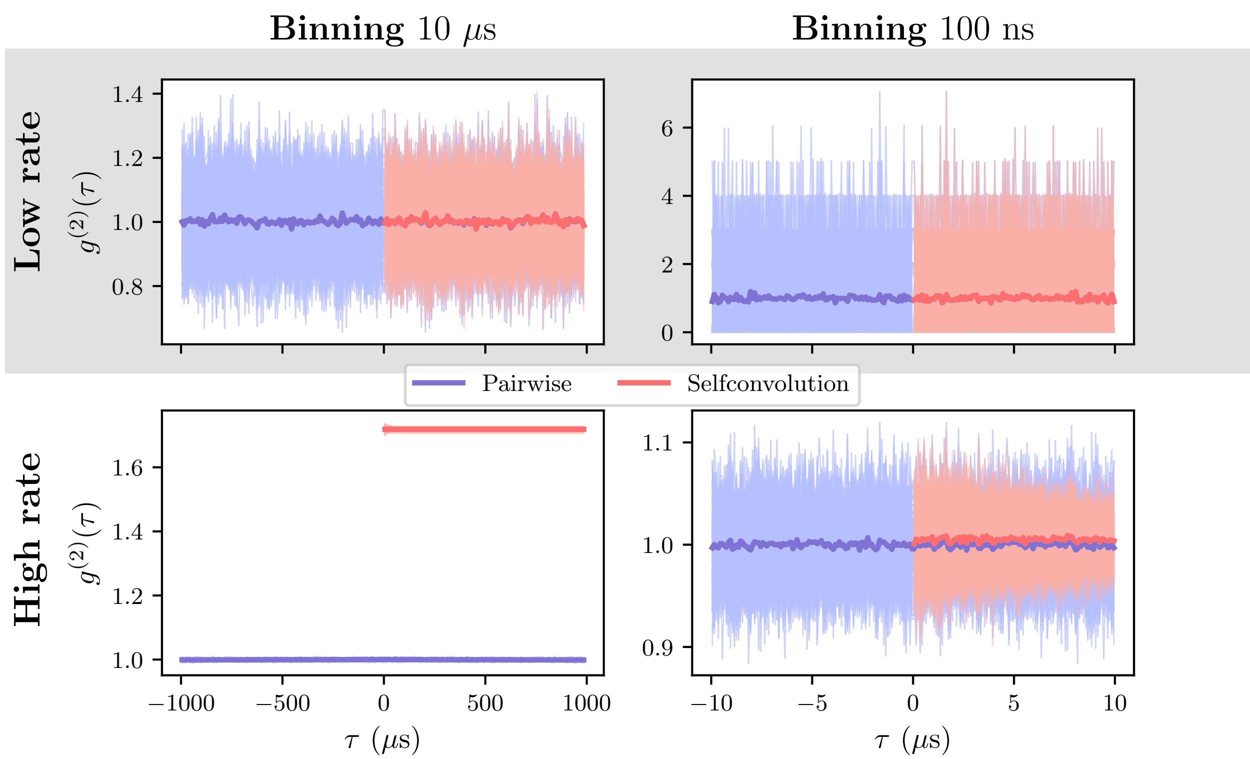

Figure 3.7: **Binning and photon rate effects on $g^{(2)}(\tau)$ determination.** The rows correspond to differents MPR (10^2 and 10^5 ph/s), while the columns are set for different time delay binning $\Delta\tau$ (10 μs and 100 ns). The blue and red colors correspond to the calculation with pairwise and self-convolution methods, respectively. Each plot contains the data from 150 runs and their corresponding average on darker color.

is used, while for the wide binning, the method converges erroneously to ∼1.7.

Based on the analysed datasets, lower dispersion, equivalent to better reliability in just one run, is obtained using narrow binning and high rate across both methods. Conversely, applying the same narrow binning to a low-rate dataset results in high dispersion. Furthermore, the results indicate that for the SC method, the binning width should be considerably smaller than the average waiting time to obtain accurate results. In contrast, for the PW method, the binning is irrelevant when characterising a laser source with long coherence time.

3.3.2 Thermal light

Thermal light has several properties that make it different from laser light when determining $g^{(2)}(\tau)$: first, it is chaotic, thus its simulation is more complex; second, the photon number distribution follows a geometric distribution; and third, $g^{(2)}(\tau)$ is greater than one at $\tau = 0$ and follows a Gaussian or Lorentzian distribution with a defined coherence time dependent on the temperature of the source and the light generation process [43].

As described at the beginning of this section, a simulation requires one to generate the temporal intensity profile of the source. Let us see how it is possible to obtain this from the power spectral density.

The Power Spectral Density (PSD) of a function $x(t)$ is given by [44]:

$$S_{xx}(f) = \lim_{T\to\infty} \frac{1}{T} |\hat{x}_T(f)|^2, \tag{3.13}$$

where $[-T/2, T/2]$ represents a period of time over which $x(t)$ has Fourier transform $\hat{x}_T(f)$. According to the Wiener-Khinchin theorem, the PSD forms a Fourier pair with the autocorrelation of the function $x(t)$ such that [44]:

$$S_{xx}(f) = \frac{1}{2\pi} \int_{-\infty}^{\infty} R_x(\tau) e^{-i\omega\tau} d\tau, \tag{3.14}$$

where $R_x(\tau)$ is the autocorrelation, defined as in Equation 3.1 equivalently to the first-order correlation. From this relation, it is possible to model the electric field of blackbody radiation in the time domain as [45]:

$$E(t) = \mathcal{F}^{-1} \left[(M + iN)\sqrt{S(f)} \right], \tag{3.15}$$

where $\mathcal{F}^{-1}$ is the inverse Fourier transform, M and N represent independent Gaussian random variables with zero mean and variance of one, and $S(f)$ is the PSD of the light. For blackbody radiation, the PSD is given by Planck's law as [46]:

$$B(f,T) = \frac{2h}{c^2}\frac{f^3}{exp\left(\frac{hf}{k_BT}\right)-1}, \tag{3.16}$$

where h is Planck's constant, k_B is Boltzmann's constant, f is the frequency of the light and c is the speed of light.

It is possible to show that the generation of data by means of Equation 3.15 produces the expected autocorrelation for blackbody radiation[6]; and therefore should have the same $g^{(1)}(\tau)$. Moreover, according to the **Siegert relation** for chaotic light [43]:

$$g^{(2)}(\tau) = 1 + |g^{(1)}(\tau)|^2, \tag{3.17}$$

this simulation process should yield the same $g^{(2)}(\tau)$ as blackbody radiation. The simulations in this sections are then done by following the discrete form of Equation 3.15 with $S(f)$ as in Equation 3.16 and calculating the instantaneous intensity using $I(t) = |E(t)|^2$.

As the light generated by this process would correspond to a Gaussian process, the expected lineshape of $g^{(2)}(\tau)$ is Gaussian such that [43]:

$$g^{(2)}(\tau) = 1 + exp\left(-\pi\frac{\tau^2}{\tau_c^2}\right), \tag{3.18}$$

with τ_c the coherence time.

In this case, the most critical parameter in the generation of thermal light is its coherence time, thus it is necessary that both simulation and calculation have a narrower binning than this time.

Several sources have discussed the theoretical value of the coherence time (or equivalently, the coherence length) of thermal sources; however, the final value depends on the procedure

[6]There are alternative ways to generate E(t) with the same autocorrelation. An interesting physical/computational approach is $E(t) = \mathcal{F}^{-1}(\sqrt{B(f;T)}e^{i\phi})$ with ϕ a random uniform variable corresponding to the random phase of each frequency component in blackbody radiation.

followed [47] [48].

I used the value of the coherence time for thermal sources according to:

$$\tau_c^{Thermal} = \zeta \frac{h}{k_B T}, \tag{3.19}$$

with $\zeta = 0.07$ [48] as an estimation of the coherence time for an initial simulation, and then the binning was tuned for each simulation to optimise the resolution.

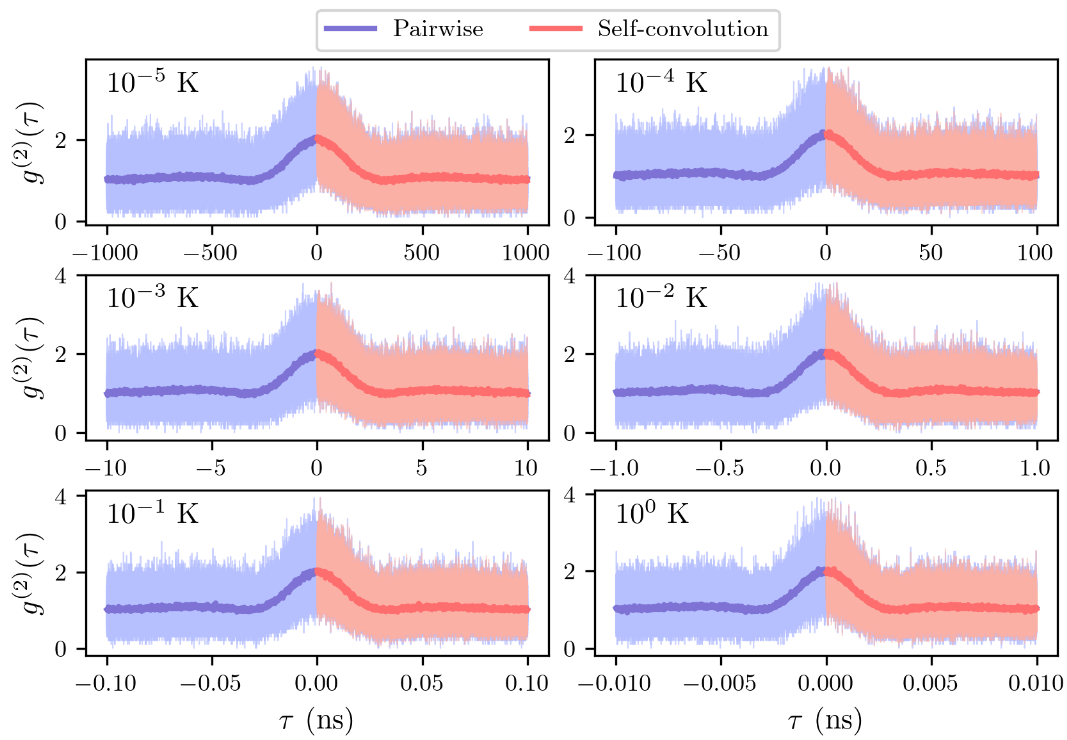

Figure 3.8: **$g^{(2)}(\tau)$ of thermal light at different temperatures.** $g^{(2)}(\tau)$ determination was done using PW and SC methods with identical results. Each plot shows the data from 150 runs and their corresponding average on darker color.

To analyse $g^{(2)}(\tau)$ as a function of temperature, I generated six distinct simulation sets, spanning six orders of magnitude from 10^{-5} K to 10^{0} K. Each configuration was run 150 times, with around 100000 photons per realisation. As every configuration required different binning, the photon rate was changed inversely to enable the data generation within a reasonable computational time. The change was such that the criterion given by Equation 3.12 was still fulfilled for every configuration.

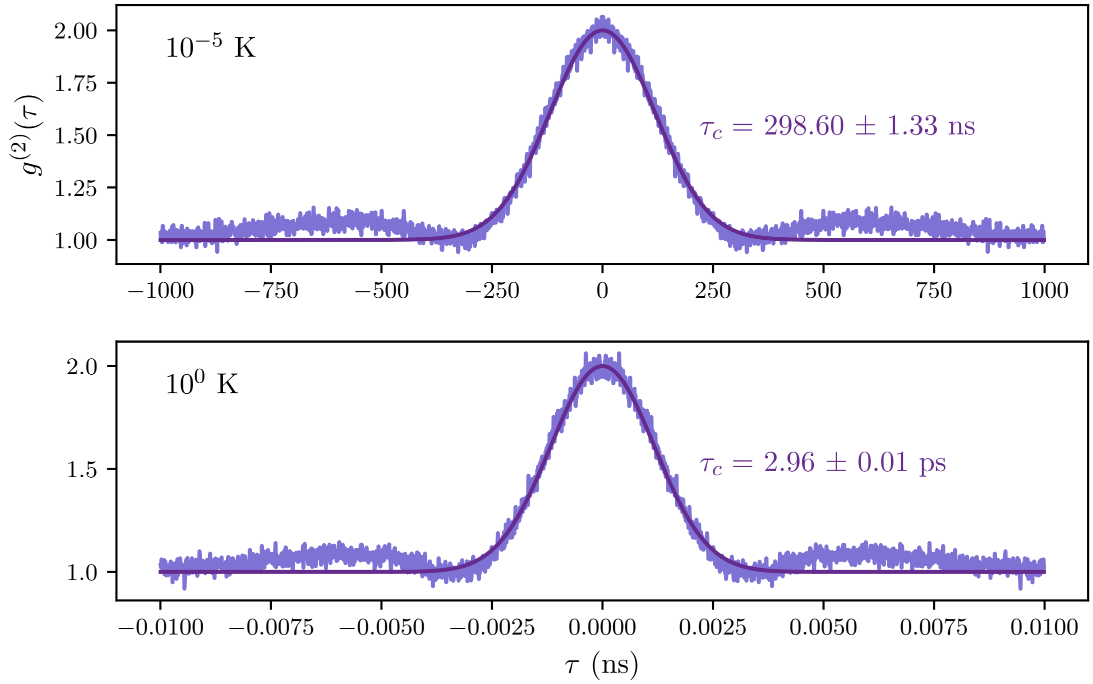

Figure 3.9: $\mathbf{g^{(2)}}(\tau)$ **of thermal light and corresponding Gaussian fit** for $T = 10^{-5}$ K and $T = 10^{0}$ K. The fitted coherence time and its corresponding statistical error is shown. It is clear that changing the temperature just scales inversely the timescale.

For each run, $g^{(2)}(\tau)$ was computed using both PW and SC methods. The individual results and their corresponding averages are presented in Figure 3.8. For the resulting average of $g^{(2)}(\tau)$ calculated by the PW method, a Gaussian fit following Equation 3.18 was performed. The fitted curves are depicted for the limiting cases in Figure 3.9. These figures show roughly the same shape, and the calculated coherence time corresponds to a scaling inversely proportional of the temperature. Besides the main Gaussian feature, additional "shoulders" are observed. The source of these shoulders is yet to be known.

The coherence times were retrieved from the Gaussian fits and plotted as a function of temperature in Figure 3.10. An inverse fit according to Equation 3.19 is shown, which yields the adjusted parameter $\zeta = 0.0618 \pm 0.0002$. Note that this value roughly resembles the one present on the literature and originally used to estimate the binning width.

Finally, an analysis of photon number distribution was done: Two configurations at

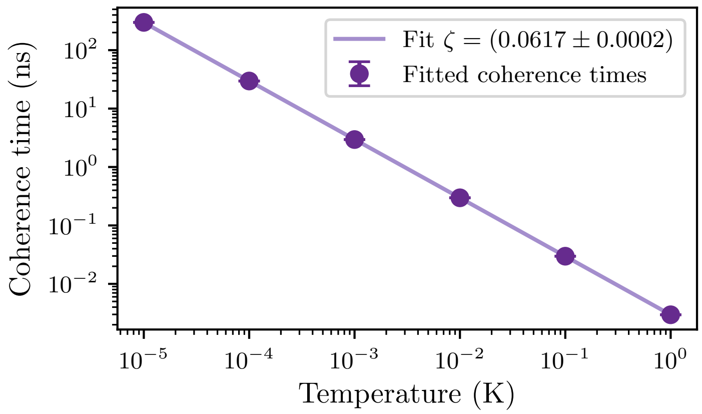

Figure 3.10: **Coherence time and temperature relation for thermal light** and inverse fit in log-log scale.

$T = 10^{-5}$ K were simulated with rates $\mathcal{R} = 10^5$ and $\mathcal{R} = 10^8$ ph/s; the time window was set as in section 3.3.1 with $n_{exp} = 5$. As seen in Figure 3.11, for low photon rates the distribution is Poissonian, while for high rates is geometrical. This difference in the behaviour can be explained in terms of the relation between the time window and the coherence time: for a time window lower than the coherence time, the bunching effects are visible and the distribution is as expected, while for greater windows than the coherence time, the decoherence of the light averages out the bunching effect, and the Poissonian sampling remains.

3.3.3 Pseudothermal light

Thermal light has intriguing properties to be studied by means of second order coherence; however, its short coherence time is troublesome: for achieving coherence times long enough to be analysed experimentally (few nanoseconds), a blackbody at $T < 10^{-4}$ K is necessary[7]. Moreover, even if a collective ensemble of atoms were to cool down to such a temperature, the total intensity would be too low to be detected.

An interesting way to achieve $g^{(2)}(0) > 1$ while working with experimentally reasonable coherence times is to consider pseudothermal light. This type of light is chaotic and the coherence time is easily tunable experimentally. More details about it are given in section 3.4;

[7]That's less than the Doppler cooling limit of the blue transition for ^{88}Sr!

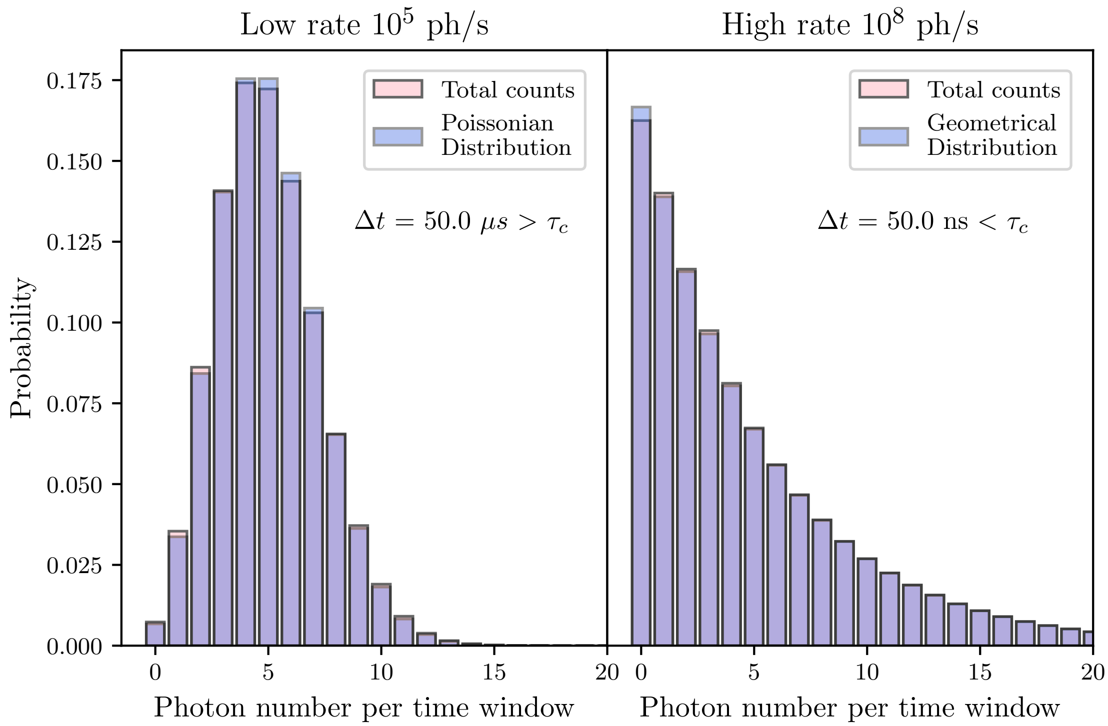

Figure 3.11: **Photon number distribution regimes for thermal light at $\mathbf{T = 10^{-5}}$ K**. A clear effect on the chosen time window with respect to the coherence time $\tau_c = 296$ ns is seen. For a window above the coherence time, there is no photon bunching and the behaviour is Poissonian, while for values below, the photon bunching of the thermal light is clearly visible. In both cases, the counts and the model overlap to good agreement.

meanwhile, let us focus on the mathematical properties of Gaussian pseudothermal light.

The temporal intensity profile can be obtained from the power spectral density as in the previous section; therefore, let us deduce the PSD for pseudothermal light.

In general, a Gaussian chaotic light source follows [43]:

$$g^{(1)}(\tau) = exp\left(-i\omega_0 t - \frac{\pi}{2}(\tau/\tau_c)^2\right), \tag{3.20}$$

with ω_0 the central frequency of the light. According to the Wiener-Khinchin theorem, this quantity is related to the PSD by [44]:

$$S'(\omega) = \mathcal{F}(g^{(1)}(\tau)) = \frac{1}{2\pi}\int_{-\infty}^{\infty} |g^{(1)}(\tau)|e^{-i\omega\tau}d\tau, \tag{3.21}$$

where the norm of $g^{(1)}(\tau)$ has been used, as the carrier wave only contains information about the phase. By replacing Equation 3.20 into this last expression, solving the integral as a Gaussian integral and substituting the definition of angular frequency $\omega = 2\pi f$, the PSD of Gaussian pseudothermal light is found to be:

$$S'(f) = \frac{\sqrt{2}}{2\pi}\tau_c \exp\left(-2\pi f^2 \tau_c^2\right). \tag{3.22}$$

As we work with Gaussian pseudothermal light, the process described by Equation 3.15 to produce a realisation of $E(t)$ is appropriate, and the same procedure as before is followed with $S'(f)$ instead of $B(f;T)$.

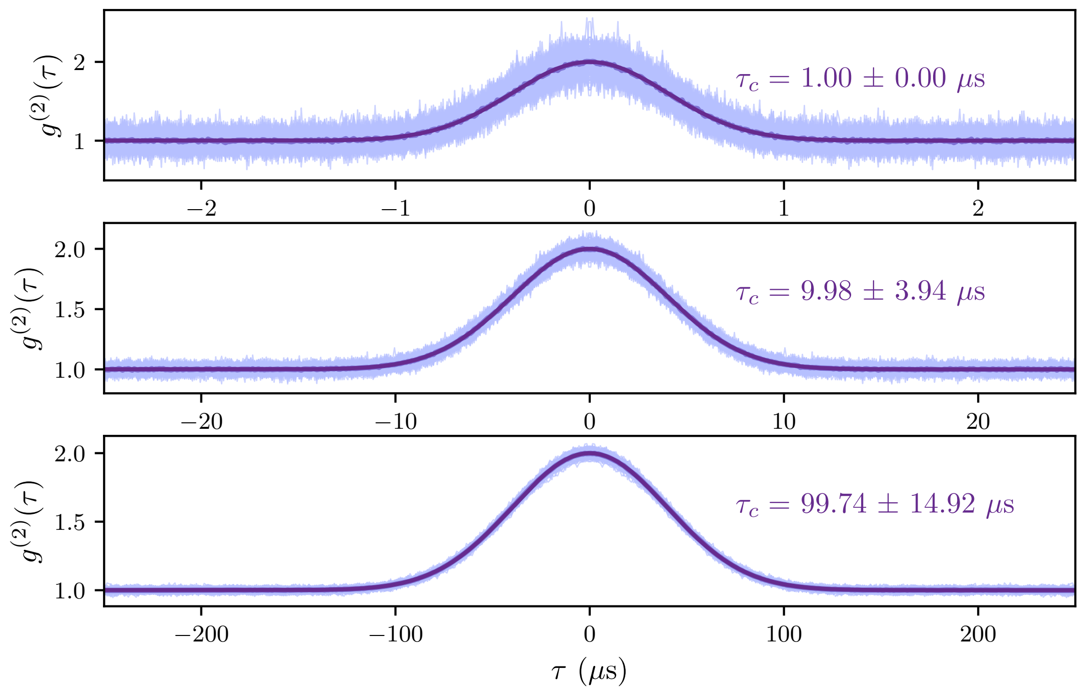

Figure 3.12: **Pseudothermal light $\mathbf{g^{(2)}}(\tau)$ and corresponding Gaussian fit** for set coherence times of 1, 10 and 100 μs from up to below. The fitted coherence time and its corresponding statistical error is shown. The fitted coherence time matches the expected value with a relative error $< 0.5\%$.

Finally, since pseudothermal light also obeys the Siegert relation[8] (Equation 3.17), the

[8]While some recent studies suggest that analysing deviations from the Siegert relation offers an experimental

functional form of $g^{(2)}(\tau)$ is identical to that of Equation 3.18. This relation indicates that the coherence time of the pseudothermal light simulations can be set in $S'(f)$ and then retrieved by fitting $g^{(2)}(\tau)$: a very convenient approach to check if the calculation methods yield the correct $g^{(2)}(\tau)$.

A first set of configurations was simulated to check that the correct coherence time and shape were obtained. For this, three coherence times—1 μs, 10 μs and 100 μs—were chosen, and simulations were run for each coherence time with same rate $\mathcal{R} = 10^5$ ph/s and binning of 100 ns. Each configuration was run 150 times with approximately 100000 photons per realisation.

The results are depicted in Figure 3.12. In each case, the retrieved coherence time matched the originally set with relative error between 0 and 0.5 %, contained within the statistical error of the fitting. In comparison to the thermal case, shown in Figure 3.9, there are no unexpected correlations beyond the one at $\tau = 0$.

To further validate the coherence time fitting, the simulations of this section are used to examine the behaviour of the SC method when the convergence condition (Equation 3.12) is violated. For this purpose, two types of simulations were performed: one at a photon rate $\mathcal{R}_1 = 10^4$ ph/s and the other at $\mathcal{R}_2 = 10^5$ ph/s, both sharing the same coherence time $\tau_c = 10\,\mu$s. Note that $\mathcal{R}_2$ does not follow the convergence criterion. Each configuration was run 150 times, with around 100000 photons per realisation.

The results are presented in Figure 3.13. As expected, the low-rate simulations yield identical results for both calculation methods; however, at higher rates, the self-convolution method fails and gives a different shape than the expected. Moreover, it is observed that at higher rate, the variance between runs is lower for both methods.

method to distinguish true thermal light from pseudothermal light, the simulation results show no such violation.

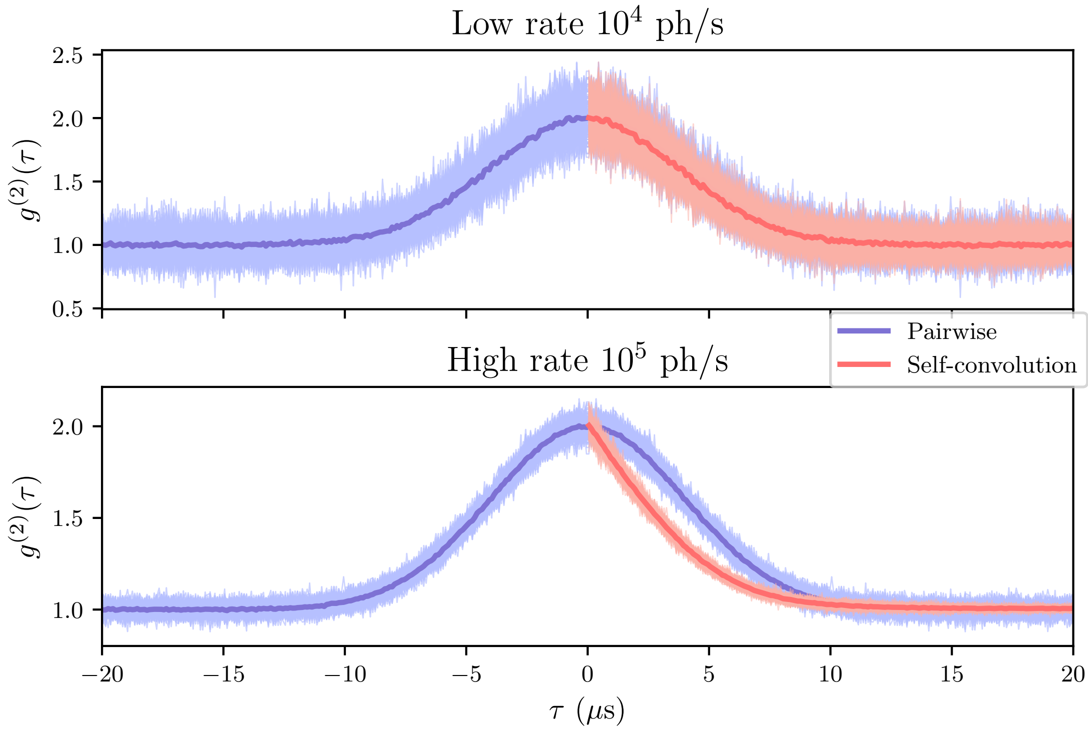

Figure 3.13: **Pseudothermal light $\mathbf{g^{(2)}}(\tau)$ for two different photon rates** calculated by PW and SC methods. Both methods are in agreement for the lower rate; however at higher rates self-convolution method fails to successfully determine $g^{(2)}(\tau)$ due to the convergence criterion. Each plot shows the data from 150 runs and their corresponding average on darker color.

3.3.4 Superradiant light

As the final purpose of the methods implementation is to characterise the superradiant laser, it is interesting to analyse the value of $g^{(2)}(\tau)$ of a superradiant source. Here I describe briefly the process that should be followed for such a task.

Consider the photon number of a superradiant laser as described in [32], focusing on the output instead of the intra-cavity photon number. The method is based on finding the solution of the number operator as $\hat{n} = b^\dagger b$, based on the creation and annihilation operators that can be found by solving the system of differential equations:

$$i\frac{d\langle b\rangle}{dt} = g\sum_j \left\langle s_j^-\right\rangle - \frac{i}{2}\kappa\langle b\rangle$$

$$
\begin{aligned}
i\frac{d\left\langle b^{\dagger}\right\rangle}{dt} &= -g\sum_{j}\left\langle s_j^{+}\right\rangle - \frac{i}{2}\kappa\left\langle b^{\dagger}\right\rangle \\
i\frac{d\left\langle s_j^{-}\right\rangle}{dt} &= -2g\langle b\rangle\left\langle s_j^{z}\right\rangle \\
i\frac{d\left\langle s_j^{+}\right\rangle}{dt} &= 2g\left\langle b^{\dagger}\right\rangle\left\langle s_j^{z}\right\rangle \\
i\frac{d\left\langle s_j^{z}\right\rangle}{dt} &= g\langle b\rangle\left\langle s_j^{+}\right\rangle - g\left\langle b^{\dagger}\right\rangle\left\langle s_j^{-}\right\rangle,
\end{aligned}
$$

by solving (for example, using Runge-Kutta methods) for a system where the atoms, with their associated s_j^i, are replaced periodically and randomly. The resulting photon number can then be associated with the output of the cavity through the leakage rate $n_{out} = \kappa n_{intra}$, and the resulting $g^{(2)}(\tau)$ can be calculated using the methods explored previously.

3.4 Experimental methods

As discussed previously, experimental determination of $g^{(2)}(\tau)$ may be done using an HBT setup with single-photon detectors and then processing the data with any of the previous methods. In this section, the experimental setup designed and built for this thesis is shown. Such implementation is based on one single-photon detector and a setup to produce pseudothermal light is also included as a way to validate the experimental method.

3.4.1 Detector considerations

Research on higher-order coherence was originally motivated by the experimental results obtained by Hanbury Brown and Twiss using their HBT interferometer [49]. Although the original experiment enables the determination of the correlation, such a setup is only required for being able to detect simultaneous photon arrivals. While such a property is desired, it is not absolutely necessary to determine the form of $g^{(2)}(\tau)$ at $\tau \neq 0$. Let us discuss the properties of single-photon detectors and their implications on determining $g^{(2)}(\tau)$.

There are several types of single-photon detectors, such as photomultiplier tubes (PMT), superconducting nanowire single-photon detectors (SNSPD), and **single-photon avalanche diodes** (SPAD), each of them with different characteristics regarding dead time, detection efficiency, jitter and implementation details [50]. These characteristics are described in table 3.2.

Of particular interest are single-photon avalanche diodes, as they usually have a high detection efficiency (up to 80%), achieve low dark count rates (down to 5 counts per second, or cps), low afterpulsing ($< 1\%$), low dead time (< 50 ns), and work at room temperature (unlike SNSPDs, which require cryogenic cooling). Additionally, they are compact and commercially available [50]. Considering these characteristics and the limitations shown in table 3.2, the detector limits the determination of $g^{(2)}(\tau)$ for experiments with low signal, as it may not be resolved from the noise, or signals with coherence times close to the dead time or the detection jitter of the detector.

Table 3.2: **Characteristics of single photon detectors.** The descriptions are mainly based on [50].

Parameter	**Description**	**Effect on $g^{(2)}(\tau)$**
Dead Time t_D	Minimum time the detector remains inactive after a detection.	Forces $g^{(2)}(\tau) = 0$ at delay times below the dead time.
Afterpulsing (AP)	Probability of triggering a false count after a detection event.	Creates a non-physical peak (artificial bunching) on $g^{(2)}(\tau)$ at short delay times ($\tau \approx t_D$).
Detection Jitter	Temporal uncertainty in the registration of the photon arrival time.	None for coherence times considerably longer than the jitter.
Detection Efficiency (PDE)	Probability of a photon triggering a detection event.	Affects signal to noise ratio (SNR). Critical for low signals.
Dark Count Rate (DCR)	Dark triggers not related to photon absorption.	Affects SNR. Critical for low signals.
Max. Count Rate	Maximum number of photon counts per unit time before saturation.	High-photon rates over the max. count yield wrong results for $g^{(2)}(\tau)$ [51].

Importantly, limitations related to the detector dead time, afterpulsing and dark counts may be easily overcome by using a two-detector setup. However, for signals characterised by long coherence times and moderate photon rates, a single-detector configuration yields accurate measurements of $g^{(2)}(\tau)$ with one detector. Moreover, experimental setups with two detectors imply increased complexity due to the necessity to align an additional detector [52][53].

Given these considerations, and keeping in mind that on the superradiant laser the target intensity is 50 pW ($> 10^8$ cps) with expected dynamics on the scale of microseconds, a single-detector scheme with few nanoseconds dead time and standard PDE and DCR performance is sufficient to resolve the temporal evolution of the system.

3.4.2 Characterisation setup

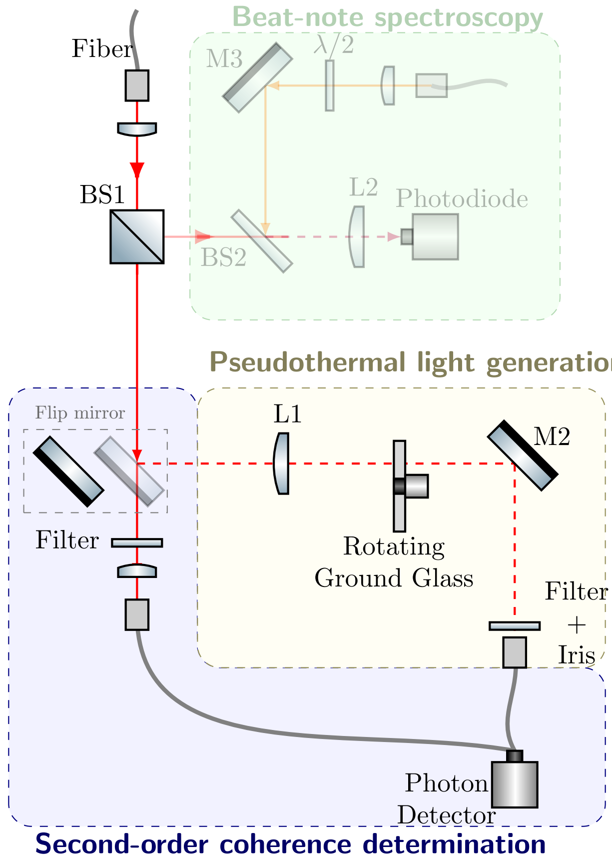

Figure 3.14: **Experimental setup for second-order coherence measurements**. Light from a fiber is collimated and subsequently split by a beamsplitter. The transmitted light can follow two different paths: in the blue section, it passes through ND-filters and is coupled to an SPAD, so the incoming light field can be characterised. In the yellow section, selected by switching a flip mirror, the light is focused onto a rotating ground glass (RGG) disk, attenuated by ND-filters, and gets onto the SPAD, so it can be used as pseudothermal light source for benchmarking.

Figure 3.14 shows the diagram of the implemented single-detector characterisation setup. The setup includes a Martienssen lamp used for pseudothermal light generation [54].

In this setup, the light to be analysed must be coupled to the input fiber, which is used to introduce the light on the system (upper left corner in Figure 3.14).

The light is then collimated, and directed towards a 90:10 non-polarising beamsplitter used for attenuating the light and splitting it. The reflected light can be used on the second part of the setup as discussed in chapter 4.

Table 3.3: **Components of the $g^{(2)}$ experimental setup.** List of optical elements used in the characterisation setup.

Element	**Description**	**Purpose**
Input fiber	Single-mode polarization-maintaining fiber (P3-630PM-FC).	Transmits sample light (testing or superradiant light) to the characterisation setup.
Input collimator	Aspherical collimator lens, $f = 5.5$ mm (C105TMD-B).	Collimates input light.
Beamsplitter BS1	90:10 (R:T) non-polarizing beamsplitter (BS073).	Attenuates the transmitted light and splits light for frequency-domain analysis.
ND-filters	Variable attenuation.	Attenuates light to achieve target counts per second, depending on the input intensity.
Output fiber	Multimode fiber.	Transmits light from the setup to the photon detector.
Photon detector	Excelitas SPCM-AQRH-10-FC.	Single-Photon detection.
Output collimator	Aspherical collimator lens $f = 11$ mm. (A397TM)	Couples the attenuated beam into the detection fiber.
Plano-convex lens L1	Variable focal length (50, 100, or 200 mm).	Used for focusing the beam onto the ground glass disk at different distances.
Rotating Ground Glass (RGG)	Thin ground glass attached to a motor. Undetermined grain size.	Used for pseudothermal light generation.

The transmitted beam, used for coherence analysis, can then follow two different paths depending on the position of the flip mirror. If the flip mirror is retracted (blue section), the light impinges on neutral density (ND-) filters, and then is coupled by a collimator lens to a multimode fiber connected to a single-photon detector. Alternatively, if the flip mirror reflects the light (yellow section), the beam is focused by a lens onto a rotating ground glass and the resulting speckle pattern is attenuated using ND-filters before being collected by a bare multimode fiber and sent to the photon detector. More details on the components used are listed in table 3.3.

The single-photon detector in this setup is a single-photon avalanche photodiode, which is a type of avalanche photodiode (APD) with a reverse bias voltage so high that a single photon produces impact ionisation: an avalanche of electrons is generated that can easily be detected. Due to the nature of the phenomenon, the detector goes blind for an instant after the detection (dead time), and residual electrons after the dead time could trigger a second avalanche (afterpulsing).

The SPAD of the setup is an Excelitas SPCM-AQRH-10-FC, with a reported dead time of 22.8 ns, afterpulsing probability of 0.1% up to 500 ns after the original detection; and with an experimentally measured efficiency of 67.6% at 689 nm and dark count rate around 60 cps. Moreover, the setup is inside a light-tight box and the multimode fiber is wrapped with aluminium to avoid noise due to external light.

Data collection by FPGA

When a photon is detected by the SPAD, it emits a voltage pulse of 2.2 V and 10 ns width. To be able to register the pulse, an FPGA[9] was designed, programmed, and implemented in collaboration with the Electronic Workshop of LPL. Figure 3.15 shows the prototype of the board.

A script was used to detect incoming pulses in "in pulse". The time between consecutive pulses is measured in ticks of the FPGA internal clock, set at 300 MHz, for a time resolution of 3.33 ns. This time difference is then temporarily saved in memory using FIFO[10] structures and then transmitted over USB using the UART[11] protocol.

There are two main bottlenecks in this process: first, USB transmission is slow, and second, there is a maximum memory on the FPGA. By decreasing the size of the variable

[9] Field-programmable gate array, typically used for dedicated hardware solutions.
[10] First-In First-Out, a type of data structure describing how the information flows in it.
[11] Universal asynchronous receiver-transmitter, one of the standard serial communication protocols.

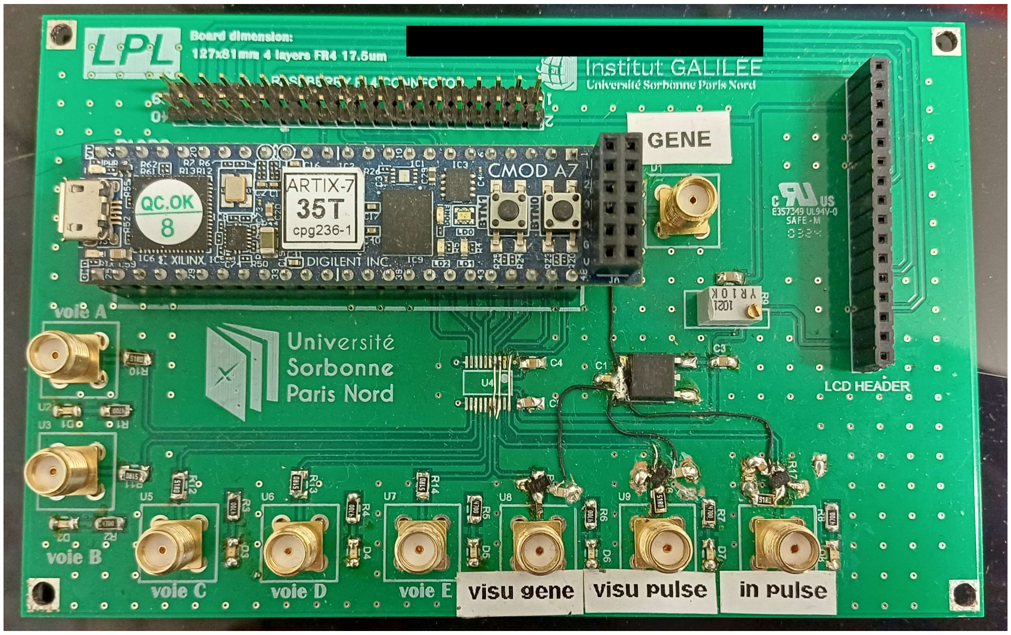

Figure 3.15: **FPGA for pulse detection and digitalisation**. The pulses generated by the SPAD are transmitted to the FPGA into the "in pulse" connector. The "visu pulse" generates a duplicate of the incoming pulse for external visualisation or counting. "Gene" and "visu gene" connectors are used to generate pulses for testing purposes. All the other SMA connectors are not used.

containing the time difference, the transmission is faster, and the number of time delays that can be saved in memory higher. However, the maximum time difference that can be stored is decreased as a consequence. Under this consideration, the size of the variable was chosen to be 32 bits, the baudrate was set to 12 Mbps, allowing for a maximum time difference around 14 s and a maximum transmission rate through USB of approximately 240000 counts per second, which means that if there are detections over this limit, the system saturates and some time differences are lost.

In addition to the FPGA, a photon counter is connected to the "visu pulse" port with a collection time of one second, so an estimation of the counts per second is acquired in place.

In the last section of the data collection process, the information sent by the FPGA is received into a computer and processed using a Python program. This program sets the number of pulses to be detected, transforms the ticks into time, and saves them in a file to be processed afterwards.

Second-order coherence measurement protocol

For a given light source, the data collection and processing for determining the second-order coherence follow these steps:

1. Inject the input light into the fiber connected to the SPAD.
2. Set up ND-filters in front of the fiber input such that the photon rate is less than 240000 cps.
3. Set up the number of counts to be collected in the Python program for data collection.
4. Start measurement.
5. Process the acquired photon arrival delays using the same code implemented in section 3.3.

3.5 Experimental validation

As in Section 3.3, a validation of the experimental setup is necessary. For that task, two types of light source were analysed: a laser source, with expected $g^{(2)}(\tau) = 1$, and a pseudothermal light source.

3.5.1 Laser light

Laser light from a tunable laser Toptica DL Pro at 689 nm is injected in the input fiber shown in Figure 3.14. The position of the flip mirror is set such that the laser beam follows the path of the blue section, corresponding to second-order coherence determination.

The laser was set at 39.2 mA, which is above the lasing threshold at 36 mA, and ND filters were inserted with a combined optical density of 9 OD for an estimated photon rate of 130000 cps. Eleven datasets of 100000 counts were taken, and the processing was done using the pairwise method with two different binning widths. The datasets were processed without modification, but afterpulse removal (AP removal) was also considered: time differences below 100 ns were removed, as they were expected to be significantly affected by afterpulsing, as it was later verified experimentally.

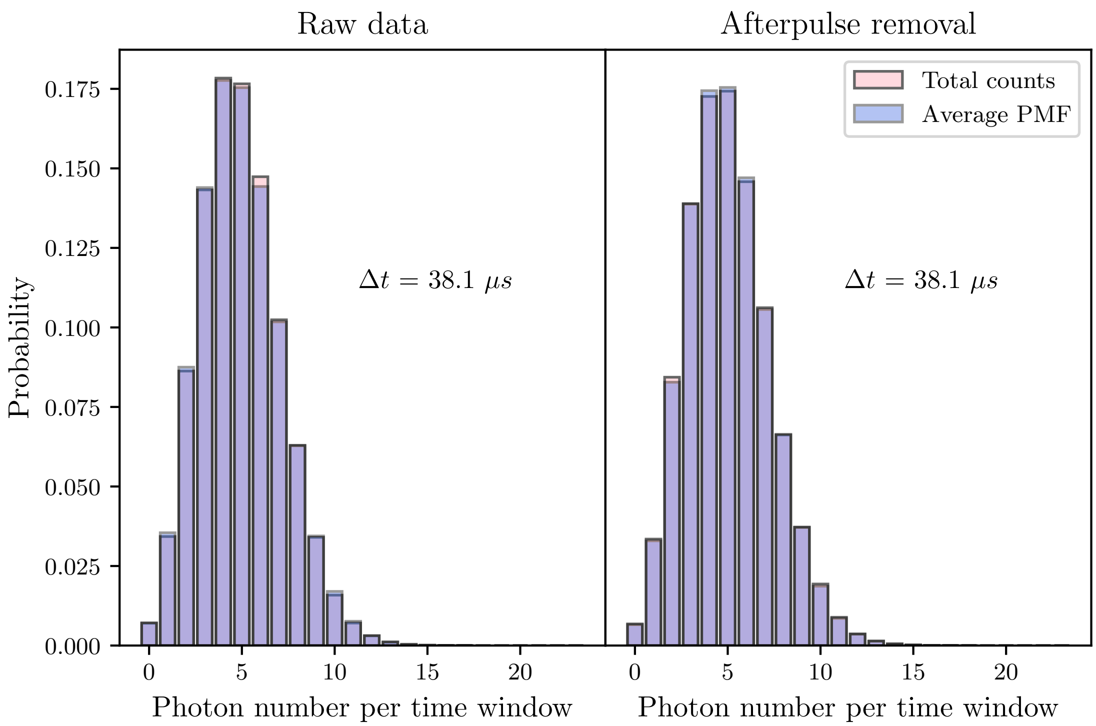

Figure 3.16: **Photon number distribution per time window for a laser source.** Raw data and AP-removal data are analysed. The average of the data and the average corresponding Poissonian Probability Mass Function (PMF) overlap as shown in the figure.

Figure 3.16 shows the photon number distribution with a expected number of photons per time window of $n_{exp} = 5$ for raw and AP-removed data along with a Poissonian PMF. As in the simulations, the PMF matches the data, either with or without AP-removal, and there are no considerable differences between the two datasets. Figure 3.17 shows the experimental $g^{(2)}(\tau)$ using the pairwise method at two distinct binning widths: the highest temporal resolution (3.33 ns) and roughly the detector dead time (20 ns). The self-convolution method was omitted due to the convergence issues identified during the simulation phase.

As seen in Figure 3.17, the second-order coherence follows $g^{(2)}(\tau) \simeq 1$ at long delay times across all analysed cases. For the high-resolution binning, a high variance between

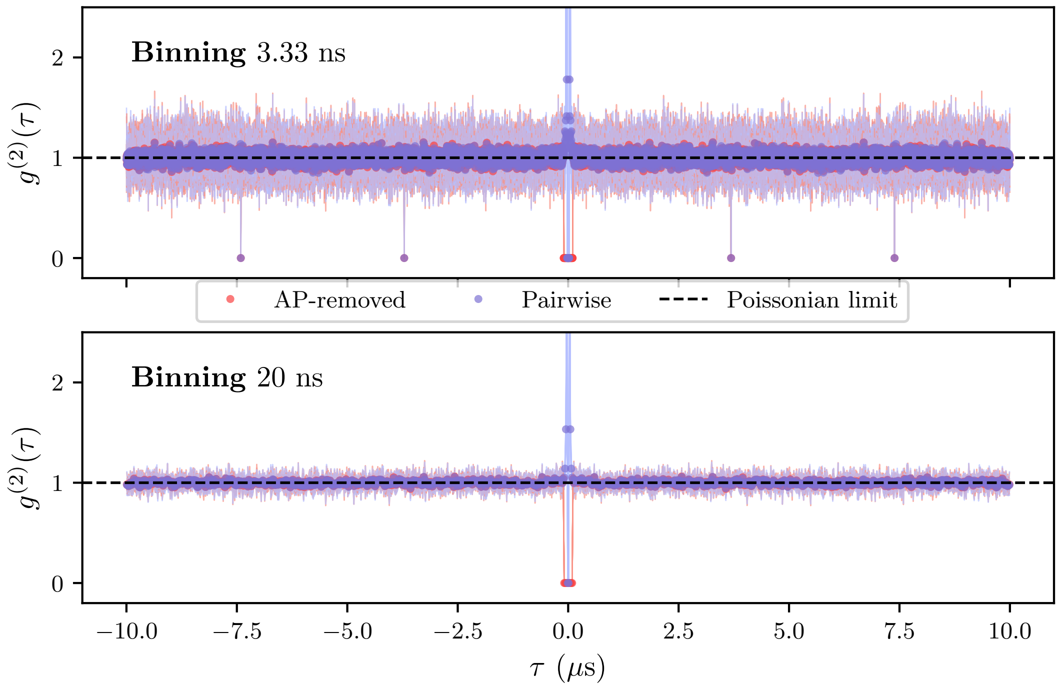

Figure 3.17: **Experimental $g^{(2)}(\tau)$ of a laser source** for different binning using PW processing. For low bin size, high dispersion is observed, and artifacts at specific time delays are present. Raw experimental data and AP-removed is shown. AP-removal provokes a dip at $\tau <$ afterpulsing time. Each plot shows the data from eleven measurements and their corresponding average on darker color. Maximum $g^{(2)}(\tau)$ value shown is 2.5, as higher values come from afterpulsing.

measurements was observed. Furthermore, sharp drops to $g^{(2)}(\tau) = 0$ appeared periodically with a period of $\tau \approx 3.7$ μs. This behaviour is most likely a hardware or data-processing artifact rather than a physical phenomenon. At delay times close to zero, the raw data exhibits high peaks in $g^{(2)}(\tau)$ (with values up to 14, not shown in the figure) centered around multiples of the detector dead time (~ 23 and ~ 47 ns), while for values lower than the dead time $g^{(2)}(\tau)$ is equal to zero. Conversely, for the AP-removed data, $g^{(2)}(\tau)$ is forced to zero for τ below the defined afterpulse time (100 ns in this case). For the 20 ns binning, the same characteristics are seen, with the main difference being the absence of the periodic artifact, and lower value of $g^{(2)}(\tau)$ due to afterpulsing (up to 4, not shown in figure).

From this analysis, it is evident that removing afterpulsing by discarding all delay times below a given threshold yields no additional benefit over simply ignoring the measured $g^{(2)}(\tau)$ values within that region.

3.5.2 Pseudothermal light (PW method)

As mentioned in the previous sections, thermal light has interesting properties to be analysed using second-order coherence, but its coherence time is too short for any easy experimental implementation. Under that consideration, it is common to analyse pseudothermal light instead.

One of the most common techniques to generate pseudothermal light is using a Martienssen lamp, where a laser beam is focused on a ground glass attached to a motor, and the forward scattered light acts as pseudothermal light [54].

More recent research on the second-order coherence of pseudothermal light has shown its behaviour in terms of shape of $g^{(2)}(\tau)$, value at $\tau = 0$ and coherence time depending on the experimental parameters of the setup. Particularly, the coherence time of Gaussian pseudothermal light is found to be related to the rotation speed of the ground glass according to [55]:

$$\tau_c = \frac{W_0}{v_t\sqrt{\left(1+\frac{F}{L}\right)^2 + \left(\frac{\pi W_0^2}{\lambda L}\right)^2}}, \tag{3.23}$$

where W_0 is the radius of the beam waist at its focus, v_t is the tangential velocity of the ground glass at the laser spot position respect to the center of rotation, and the distances F and L are as shown in Figure 3.18.

Equation 3.23 comes from the physics behind the pseudothermal light generation: as the light hits the ground glass, it generates a speckle pattern behind it with some maxima and some minima that are randomly spatially distributed. As the ground glass moves, this pattern gradually changes at a speed that depends on the size of the speckle on the fiber and the rotation speed.

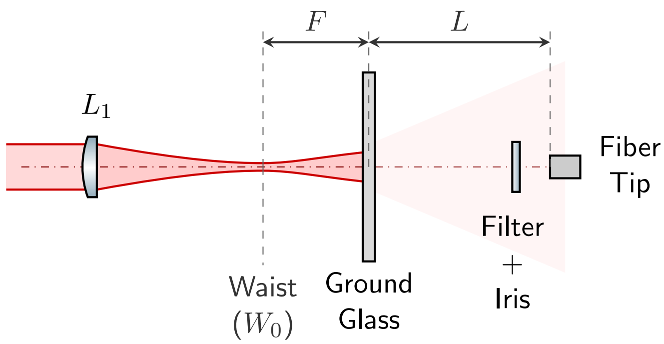

Figure 3.18: **Pseudothermal light setup.** A laser beam is focused using a lens L_1 towards a rotating ground glass. The inhomogeneous surface produces a changing speckle that is partially collected by a multimode fiber, acting as pseudothermal light. The properties of the light depend on the original light, the beam waist W_0, the distance between the beam waist and the ground glass F and the distance between the glass and the fiber tip L.

Note that Equation 3.23 follows a different definition for the coherence time of Gaussian thermal light:

$$g^{(2)}(\tau) = A + B \exp\left(-\frac{\tau^2}{\tau_c^2}\right), \tag{3.24}$$

where A and B are fitting constants, as several phenomena may change the value of $g^{(2)}(0)$ or its baseline [55]. Also note that the coherence time is different from that defined by Equation 3.18.

For the experimental validation with pseudothermal light, a Martienssen lamp was built using a Toptica DL Pro laser at 689 nm, combined with a ground glass disk prepared by the Optical Workshop at LPL and attached to a chopper motor (controlled by an SR540 chopper controller). In this setup, the original chopper wheel was removed; therefore, the controller could not measure the rotation frequency of the motor.

To be able to relate the coherence time and the rotation speed using the Equation 3.23, the latter one must be determined. For this, a small piece of black tape, as shown in Figure 3.19, was placed on the ground glass, such that the photon rate was modulated and the rotation frequency could be retrieved by Fourier analysis. The effects of the tape were analysed and the only effect for maximum τ below the rotation period is related to a slight increase in the

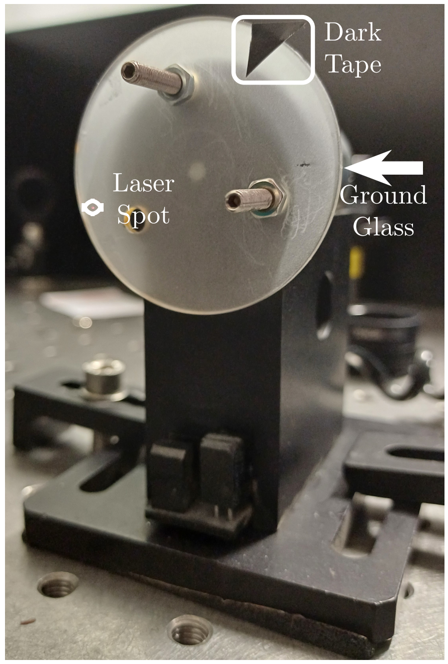

Figure 3.19: **Rotating Ground Glass** attached to the chopper motor. A black tape is taped on the surface for signal modulation.

value of $g^{(2)}(0)$.

A plano-convex lens L1 with focal length $f = 99.7$ mm was set in the setup shown in Figure 3.14. The ground glass was placed at $a = 95$ mm from the lens, the detection fiber was set at $L = 435$ mm, and the distance between the center of the RGG and the laser spot was measured to be 19 mm. Under this configuration, experimental data of photon arrivals was taken for different rotation speeds ranging from the minimum stable speed to the maximum of the motor.

For each rotation speed, $g^{(2)}(\tau)$ was calculated using the pairwise method to avoid convergence issues, and a Gaussian fit was performed according to Equation 3.24. An example of the experimental data with its corresponding fit is shown in Figure 3.20. The experimental data showed higher dispersion at higher frequencies, mainly related to the time resolution. Conversely, lower frequencies showed a worse fit to a Gaussian curve. Its behaviour may be closer to a Voigt profile, and it may not be directly related to the lower frequency, but rather to the lower noise level.

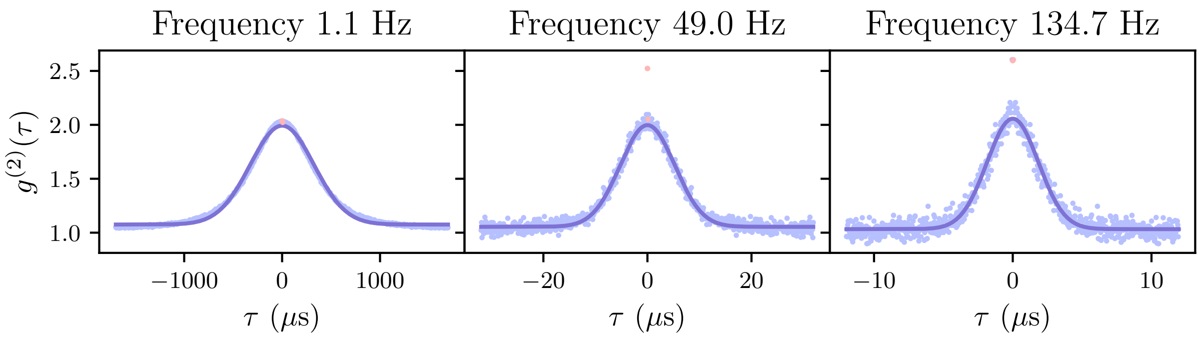

Figure 3.20: **Experimental** $g^{(2)}(\tau)$ **of a pseudothermal source** for different rotation speeds. Experimental data and Gaussian fit is shown. For the Gaussian fit, the red dots were excluded as they might be affected by afterpulsing.

Figure 3.21 is built using the measurement of the rotation speeds and their corresponding fitted coherence times, compared against theoretical curves derived from Equation 3.23. To validate the experimental data, two distinct approaches were employed to determine the beam waist radius W_0 and its distance F to the rotating ground glass.

First, an *ab-initio* approach was used by taking the mode field diameter (4.5 μm at 630 nm, as reported by the manufacturer) at the output of the fiber, and propagating the beam using ABCD matrices to calculate the waist parameters ($W_0 = 46.6$ μm, $F = 2.74$ mm). The resulting values yield the blue curve in Figure 3.21.

Alternatively, the beam diameter was measured along both axes at different distances after the lens L1 using a beam profiling camera. These diameters were fitted to a Gaussian beam propagation model to extract the experimental horizontal waist parameters ($W_0 = 52.0$ μm, $F = 2.77$ mm), which are used to generate the red curve in Figure 3.21.

The inset in Figure 3.21 shows the residuals between the experimental data and Equation 3.23 for both approaches. In both cases, the experimental values are outside the error estimation of the models; however, they show good qualitative agreement with the theory. The residuals reach up to 90 μs at low frequencies for the ABCD matrix model, and up to 50 μs for the experimental measurement of the beam waist (not shown in figure), and then approaching zero at high frequencies for both cases. This trend aligns with the behaviour

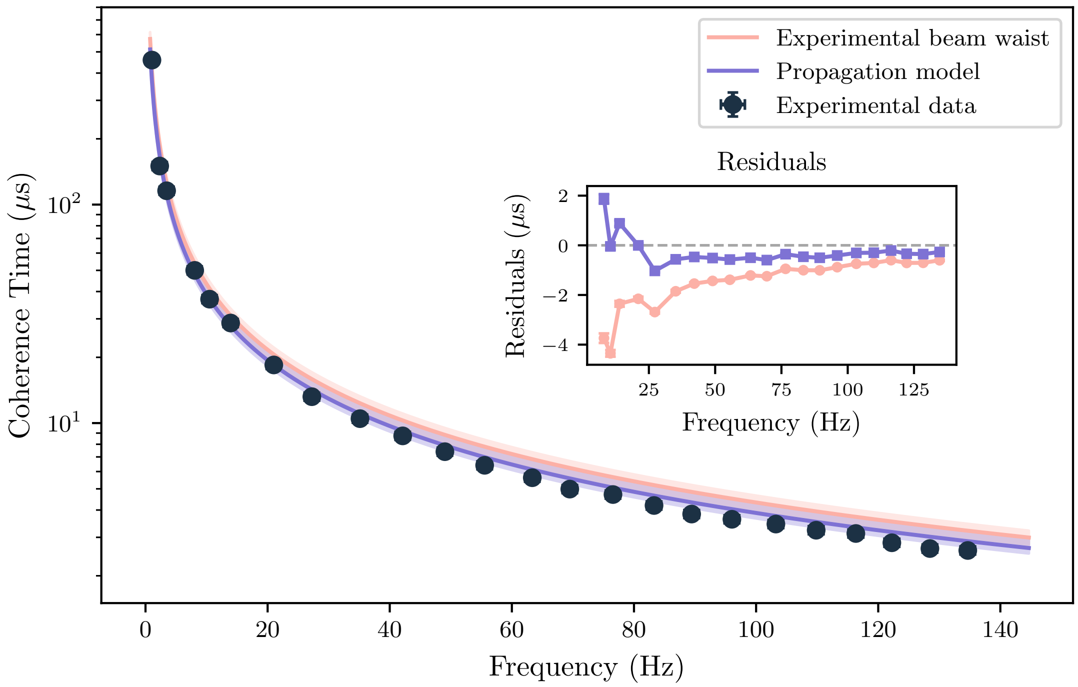

Figure 3.21: **Relation between coherence time and rotation frequency.** Experimental data corresponds to $g^{(2)}(\tau)$ Gaussian fit. Two estimations based on Equation 3.23 are shown. For the red curve, the beam waist and its distance to the ground glass plate are estimated experimentally. For the blue curve, the mode field diameter of the input fiber was taken and the propagation of the beam is done using ABCD matrices to obtain the beam waist and the position. The shaded color represents a 1-sigma error estimation for each of the curves. The inset shows the residuals between the experimental data and the models.

reported in [41], where the coherence time at low frequencies is affected by the laser linewidth. Particularly, this effect allows to deduce the laser linewidth according to [41]; however, when following the same procedure, implausible results were obtained in this case. The reason behind this remains to be understood.

Furthermore, the residuals plot shows that the experimental values tend to be below the estimations, indicating systematic errors in the measurement process, more likely related to the distances as both models depend on them.

3.5.3 Data correction for SC method

In the previous subsection, the experimental data were analysed only using the pairwise method to avoid the convergence issues related to the self-convolution method. Unfortunately, the data cannot be processed using this method as the condition given by Equation 3.12 is usually not fulfilled, because of the high count rate and the long coherence times.

Fixing this experimentally is as easy as putting an ND-filter before the input of the detector. The physical effect of the filter is that photons are selected randomly with certain probability related to the optical density of the filter. Therefore, the following question arises naturally: Is it possible to select photons randomly to lower computationally the mean photon rate and use the SC method?

In this section, I propose and implement such a "computational attenuation", and verify the results by comparing with the pairwise method. The steps are as follows:

1. Generate a list of uniformly distributed random numbers with size equals to the number of arrival times.

2. Create a mask from the random numbers based on a threshold value defined by the ratio between the intended photon rate and the experimentally measured one.

3. Apply the mask to the arrival times.

4. **Do Monte-Carlo sampling:** Repeat the process several times and retrieve the average of the resulting $g^{(2)}(\tau)$ for each sample.

The last step of the process was implemented to reduce the dispersion on the measurement, considering that low photon rates yield $g^{(2)}(\tau)$ with high dispersion. To verify the process, two of the previously taken experimental datasets were considered, with coherence times of $\tau_c^1 = 2.84\ \mu$s and $\tau_c^2 = 27.5\ \mu$s, and original photon rates of $\mathcal{R}_1 \approx 116000$ cps and $\mathcal{R}_2 \approx 121000$. The new photon rates were set to $\mathcal{R}_1' \approx 10000$ cps and $\mathcal{R}_2' \approx 2000$ cps, respectively.

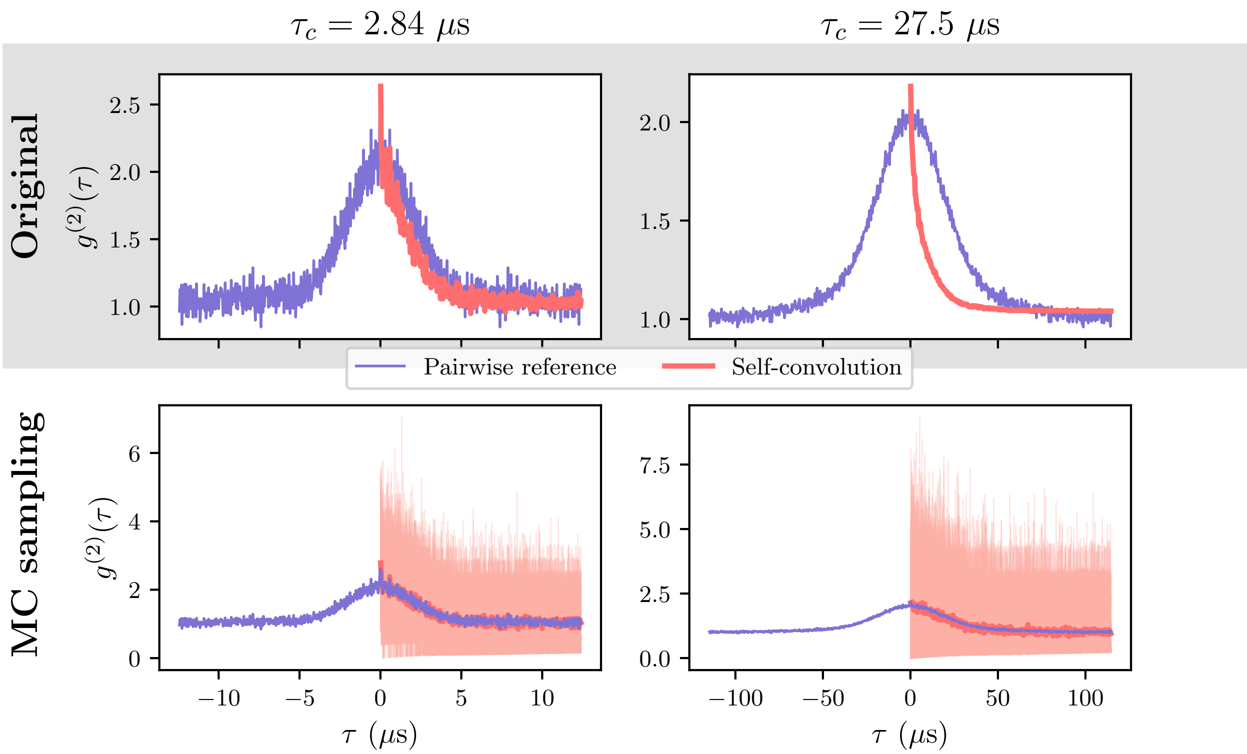

Figure 3.22: **Monte-Carlo sampling for SC method** for two different experimental coherence times. The high photon rates of the original data produced wrong results for the SC method as seen in the upper row. By computationally attenuating the photon flux and averaging, the self-convolution method approximates to the reference data as seen in the lower row. The lower row shows all the Monte-Carlo runs (on the same dataset), and the average of them in darker color.

The results of the data masking and Monte-Carlo sampling are shown in Figure 3.22. The original datasets yielded wrong values when using the self-convolution method. By following the Monte-Carlo sampling and averaging over 150 samples, the average value approximated the expected value given by the pairwise method applied to the original data. The new rates were chosen so that the resulting curve would approximate the expected response.

Note that in this case, the product of the new mean photon rate and the coherence time was lower than 0.1 for both cases. This value is smaller than the necessary one for convergence seen in Figure 3.13, which may be related to the fact that experimental data are affected by dark noise, external sources, and afterpulsing. Moreover, note this “computational attenuation" does not distinguish between photon clicks and noise; thus, the results of this technique are expected to differ from those obtained with a physical ND-filter.

Finally, although the method appears to work, the additional processing overhead makes the computation much slower, defeating the original purpose of using the self-convolution method for its speed.

Chapter 4

Frequency-domain characterisation

Spectroscopy was born as a proper scientific discipline during the 19th century due to the progress in the understanding of chemical spectra. Several physicists and chemists contributed to the interpretation of observations made several years earlier, finally concluding that the elements have characteristic spectral lines [56].

Frequency characterisation using optical spectroscopy has evolved since then, focused not only on measuring broadband spectra using passive optical elements, such as gratings and prisms, but also tailored towards high-resolution determination of wavelengths with more complex setups. For this purpose, two phenomena are usually used: interferometry and beat notes.

In interferometric techniques, the beam from a coherent light source is superimposed on a modified version of itself, generating an interference pattern defined by the parameters of the setup and the wavelength of the light [57]. While the techniques themselves yield measurements at a single wavelength, some opto-mechanical or electro-optical setups can be used to scan and explore the frequency domain and reconstruct a full spectrum.

Contrastingly, in beat note techniques, the superimposition of electric fields from different sources is used. Such a mixing generates a beating in the radio-frequency (RF) domain that can be detected using broadband photodetectors [58]. Implementation of such techniques was initially possible due to the invention of masers and lasers as high coherent sources [59], and has evolved to the current standard of beat-note spectroscopy applied to frequency combs for high-precision measurements [60].

In the context of this thesis, beat-note spectroscopy can be used to achieve a precise determination of the emission frequency and the linewidth of superradiant light. The theoretical background and experimental implementation of this technique are detailed in the following sections.

4.1 Beat-note Spectroscopy

The basic principle behind a beat-note (or heterodyne beat frequency) is rather simple. Consider two coherent monochromatic light sources with electric field of the form:

$$E_1(t) = A_1 e^{i(\omega_1 t + \phi_1)}$$
$$E_2(t) = A_2 e^{i(\omega_2 t + \phi_2)},$$

where A_i, ω_i and ϕ_i are the amplitude, angular frequency and phase for each case. The superposition of the light beams is the sum of both fields

$$\begin{aligned} E(t) &= E_1(t) + E_2(t) \\ &= \exp\left[i\left(\frac{\omega_1+\omega_2}{2}t + \frac{\phi_1+\phi_2}{2}\right)\right]\left[A_1 \exp\left(i\frac{\Delta\omega t + \Delta\phi}{2}\right) + A_2 \exp\left(-i\frac{\Delta\omega t + \Delta\phi}{2}\right)\right]. \end{aligned}$$

As in an experimental setup the instrument used for detection of light is a photodiode with a square law response, we are interested in the intensity of the resulting superposition, which is given by [61]:

$$I(t) = E^*(t)E(t) = |A_1|^2 + |A_2|^2 + 2\cos(\Delta\omega t + \Delta\phi), \tag{4.1}$$

where $\Delta\omega = \omega_1 - \omega_2$ and $\Delta\phi = \phi_1 - \phi_2$. Therefore, the beat has frequency $\Delta\omega$.

For a non-physical ideal beat, the corresponding PSD corresponds to a Dirac delta at frequencies $\Delta\omega$ and $-\Delta\omega$, while for Gaussian sources, like a laser with low-frequency noise [62], it shows a linewidth [63]:

$$\Delta f_{BN}^2 = \Delta_{f,1}^2 + \Delta_{f,2}^2, \tag{4.2}$$

where Δf_{BN} is the linewidth of the beat-note, and $\Delta_{f,i}$ is the linewidth of each source. If the sources have a Lorentzian line shape, like a laser with high-frequency noise [62], then the beat-note linewidth is just related by the direct sum [58]:

$$\Delta f_{BN} = \Delta_{f,1} + \Delta_{f,2}. \tag{4.3}$$

For a Lorentzian profile, the measured PSD can be described by [61]:

$$\boxed{S_{BN}(f) = \frac{\Delta f_{BN}}{2\pi\left[(f - f_{BN})^2 + (\Delta f_{BN}/2)^2\right]}.} \tag{4.4}$$

The frequency of the beat can be measured experimentally using an electronic spectrum analyser to obtain the Power Spectral Density (PSD) at the output of a photodiode, which must be responsive at the beating frequency. This way, there are several experimental requirements to generate and detect the beat [58]:

- **Small frequency:** The frequency of the beat must be within the bandwidth of the photodetector.
- **Polarisation superposition:** The two beams must not be orthogonal.
- **Mode superposition:** The beam modes must not be orthogonal. The spatial distribution of the beam must be partially or completely overlapped.

4.2 Experimental setup

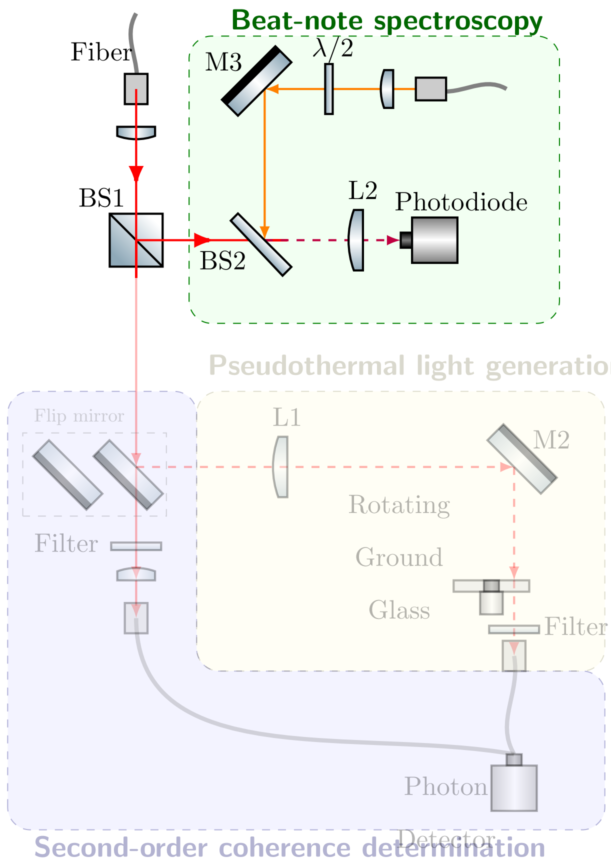

Figure 4.1: **Experimental setup for beat-note spectroscopy measurements**. Sample light from a fiber is collimated and subsequently split by a beamsplitter. The reflected part is guided towards a beam sampler BS2. Reference light from another fiber is collimated, passed by a half-wave plate and guided towards BS2. The superposition of both beams can then be focused using a convex lens L2 into a photodiode.

Figure 4.1 shows the diagram of the implemented beat-note spectroscopy setup. It is part of the larger setup including the $g^{(2)}(\tau)$ characterisation as discussed in the previous chapter.

The setup is designed to follow the standard approach for beat-note spectroscopy with one detector: two sources of light, one acting as a reference and one acting as signal, are mixed into a photodiode, with the reference light intended to be a well known stable laser, and the signal light the one to be analysed. In this setup, a half-wave plate is used at the reference input so the polarisation of one of the beams can be controlled to avoid orthogonality.

Additionally, as both input fibers are of the same type and use the same collimator, the propagation distances of both beams are approximately the same so the size of both beams matches. Finally, the superposition of the beams may be focused by a lens at position L_2.

Other heterodyne techniques are based on the use of a balanced beam sampler and a photodiode at each output. These setups have the main advantage of removing the noise of the reference beam, as it is present in both detectors and can be subtracted [64]. However, such a setup implies an additional photodiode and further alignment. If the reference signal is stable enough, a setup with an unbalanced beam sampler and a single photodiode is a cost-effective solution.

4.2.1 Photodiode response

The photodiode is a Thorlabs FDS025 integrated into a custom circuit prepared by the Electronic Workshop of LPL, with a target bandwidth of up to 240 MHz. To verify the frequency response of the photodetector, two experimental procedures were followed.

First, a Rigol DSA 815-TG spectrum analyser was operated in Tracking Generator (TG) mode. In this mode, the analyser outputs a frequency-swept signal up to 300 MHz, at the same time that measures the incoming signal in the input, thus determining the frequency response of the system. The output signal was connected to the DC-input driver of a Toptica DL pro Laser at 689 nm, modulating the outgoing light which was collimated towards the photodiode active area. The spectrum analyser then recorded the AC signal from the photodiode, corresponding to its response to the modulated beam. The resulting spectrum is shown in Figure 4.2.

A strong DC component is observed in the baseline response, leading to a lower response to real low-frequency signals as seen in the normalised response. As shown in Figure 4.2, the response is relatively stable between 70 and 210 MHz. Below 70 MHz the response is higher; however, the same behaviour holds even without laser modulation, indicating that this mid-frequency enhancement also applies to the background noise floor.

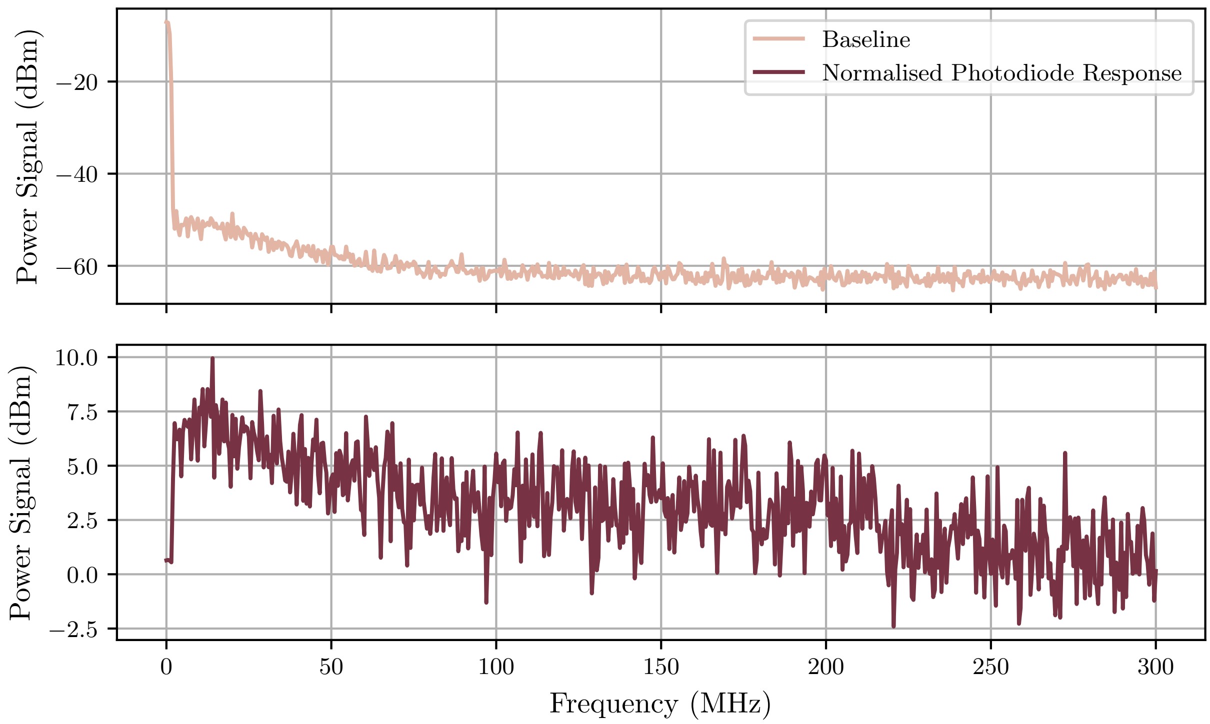

Figure 4.2: **Photodiode response with and without modulating signal.** The baseline corresponds to the photodiode signal in the absence of laser modulation. The normalised photodiode response was obtained using the TG mode of the spectrum analyser and normalised with respect to this baseline.

Second, the high-frequency detection capability of the detector was assessed. By modulating the laser signal by the DC-input driver and a Rigol DSG836 signal generator, several frequencies were tested ranging from 5 MHz up to 240 MHz. The results are shown in Figure 4.3.

These data demonstrate that the photodiode is capable of detecting this range of frequencies, making it suitable for further experimental use. Although the responsivity drops slightly at 240 MHz, the effect may be related to photodiode circuit bandwidth, as well as the modulation response of the laser DC-input.

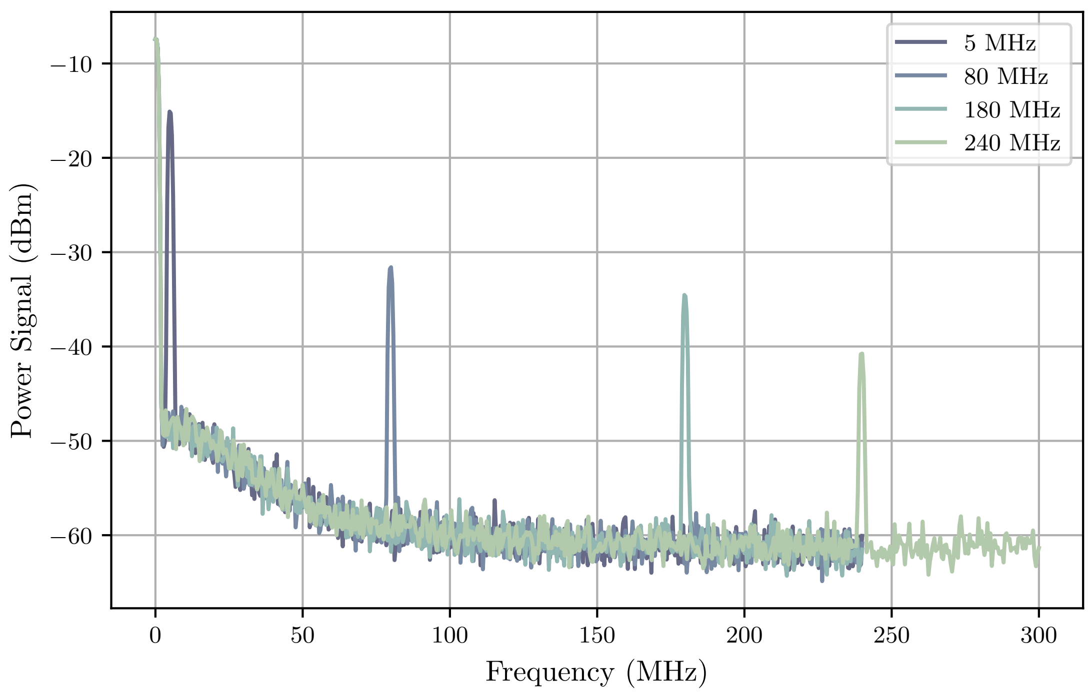

Figure 4.3: **Photodiode response at different modulation frequencies.**

4.2.2 Laser beating

As the final purpose of the beat-note spectroscopy is to be able to measure the properties of superradiant light with respect to a reference, I tested the capability to detect the beating from two independent laser sources.

In this case, the reference light was taken from the free-running Toptica DL pro laser (Sr_2 Laser) with reportedly about 20 kHz linewidth, according to the manufacturer; while the sample light corresponded to the excitation beam of the main Superradiant setup (Sr_1 Laser). This beam is intensity-controlled using acousto-optic modulators, and its frequency is locked to the $^1S_0 \leftrightarrow {}^3P_1$ transition of ^{88}Sr, corresponding to $f_s \approx 434.8290$ THz, with linewidth narrowed to about 1-2 KHz.

Regarding the reference laser, the frequency was tuned initially changing the current and checking the approximate emission frequency by measuring it with a wavemeter, and after it was determined it was close enough ($\Delta f \sim 1$ GHz) to the sample light frequency, it was further tuned using the piezoelectric module of the laser controlled by its laser controller.

Although the reference beam is usually taken as a well-defined beam, such as a frequency-locked beam, I decided to use the Toptica laser as areference as I had better control over the output intensity of this laser compared to the other.

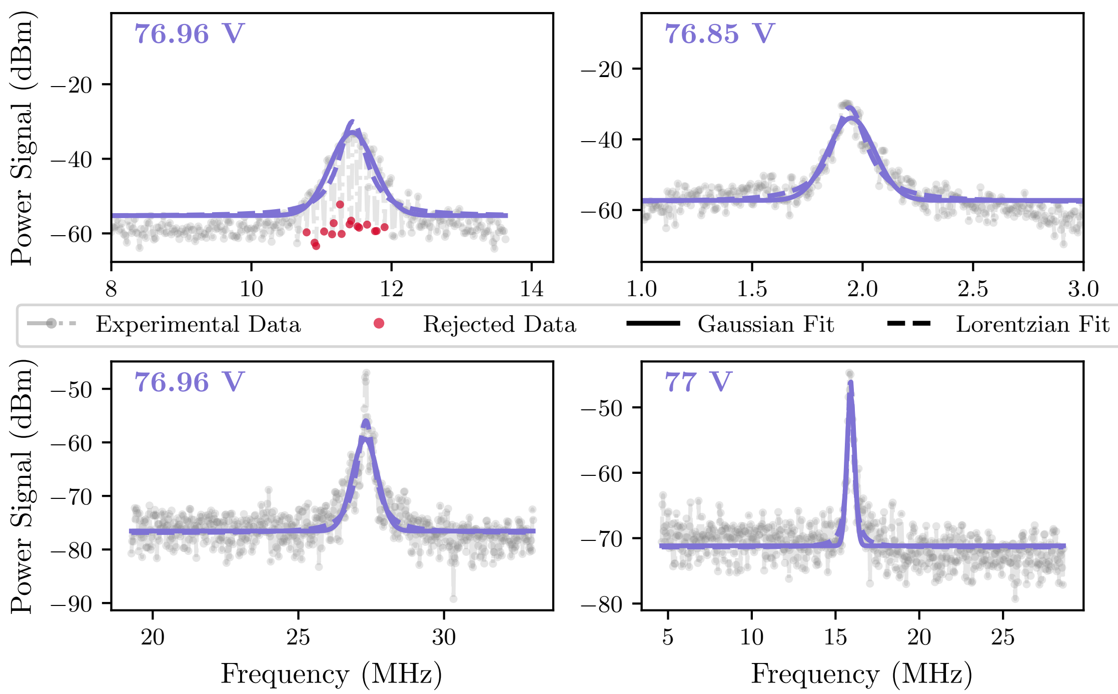

Figure 4.4: **Frequency spectrum of laser beating.** Each plot corresponds to a measurement at different time. The indicated value is the voltage applied to the piezoelectric. Gaussian and Lorentzian fits are shown.

The superposition of the beams was collimated into the active area of the photodiode without using any lens at position L_2 as the power of both beams is big enough to be detected by the photodiode without further focusing. Several spectra of the superposition were taken by changing the voltage of the piezoelectric. The results are shown in Figure 4.4. The beating changed regularly as one of the lasers was a free-running laser without any type of lock. For one of the spectra, additional beats were measured in the peak (First plot at 76.96 V). This effect may be related to a modulation of one of the lasers that was not present in the other measurements, or it was not visible due to the spectrum resolution.

Furthermore, the expected linewidth of the sources yields a beat-note linewidth between 20 and 22 kHz according to Equations 4.2 and 4.3. This value is much smaller than that obtained from the proposed fits, which all show a linewidth between 95 kHz and 370 kHz, depending on the fitting curve and the dataset. This could mean that the measurement captures the envelope of the previously mentioned modulation, while the underlying oscillations are related to the linewidth of the beat-note. Further measurements with better resolution and stabilisation of the free-running laser are necessary to confirm the origin of this behaviour.

Chapter 5

Conclusions and prospects

In this thesis, a complete computational and experimental pipeline was developed for second-order coherence ($g^{(2)}(\tau)$) and beat-note spectroscopy measurements, establishing the necessary diagnostic tools for superradiant light characterisation.

First, extensive simulations covering laser, thermal and pseudothermal light were performed to validate the computational implementation of the $g^{(2)}(\tau)$ calculation algorithms. For laser and pseudothermal light, the numerical results showed excellent agreement with theoretical models. For thermal light, the relation between temperature and coherence time was investigated, though further theoretical work is necessary to explain anomalous values of $g^{(2)}(\tau)$ beyond the coherence time.

Second, the proper functioning of the methods was also demonstrated experimentally, using both laser and pseudothermal light sources. Although a slight numerical discrepancy in coherence time was found for pseudothermal light, the qualitative behaviour closely matches theoretical prediction. This deviation was attributed to systematic distance measuring errors and the effects of the spectral linewidth of the laser. Additional research is necessary to relate the linewidth influence on the experimental measurements. Moreover, a correction process to be able to process experimental data with the self-convolution method was confirmed; however, its practical applications are limited.

Third, the primary experimental instrumentation for beat-note spectroscopy was implemented and evaluated. The photodiode was found to have roughly flat frequency response between 70 and 210 MHz, with capabilities to detect beat-notes up to 240 MHz. Furthermore, beat-note signals between a free-running laser and a frequency-locked laser were obtained, with some characteristics regarding the linewidth and shape to be further investigated.

In summary, the computational and experimental demonstrations validate the measurement pipeline on both quantities before it can be applied to superradiant light.

As future prospects, the theoretical framework will be extended to compute the expected $g^{(2)}(\tau)$ function specifically for continuous superradiant light lasing, providing a reference for experimental measurements of superradiant emission. Regarding beat-note spectroscopy, future efforts will aim to establish the intensity and frequency detection limits of the setup. Finally, connecting the experimental setup to the REFIMEVE[1] network will enable absolute frequency measurements with metrological precision. Furthermore, the beating signal can be used as a reference for active frequency-locking.

[1] Metrological Fibre Network with European Vocation, providing ultrastable, high-accuracy optical frequency standards.

Appendix A

No-plagiarism declaration

I hereby declare that this thesis and the work reported herein was composed by and originated entirely from me. Information derived from the published work of others has been acknowledged in the text, and references are given in the list of references.

Cristian Serna (2026)

References

[1] E. Betz, "Why astronomy is considered the oldest science," Oct. 2020.

[2] NIST, "A Walk Through Time - The Evolution of Time Measurement through the Ages," *NIST*, July 2009. Last Modified: 2026-02-04T10:58-05:00.

[3] BIPM, "SI unit of time (second)," 1967.

[4] M. C. Marshall, D. A. R. Castillo, W. J. Arthur-Dworschack, A. Aeppli, K. Kim, D. Lee, W. Warfield, J. Hinrichs, N. V. Nardelli, T. M. Fortier, J. Ye, D. R. Leibrandt, and D. B. Hume, "High-Stability Single-Ion Clock with 5.5×10^{-19} Systematic Uncertainty," *Physical Review Letters*, vol. 135, p. 033201, July 2025.

[5] N. Dimarcq, M. Gertsvolf, G. Mileti, S. Bize, C. W. Oates, E. Peik, D. Calonico, T. Ido, P. Tavella, F. Meynadier, G. Petit, G. Panfilo, J. Bartholomew, P. Defraigne, E. A. Donley, P. O. Hedekvist, I. Sesia, M. Wouters, P. Dubé, F. Fang, F. Levi, J. Lodewyck, H. S. Margolis, D. Newell, S. Slyusarev, S. Weyers, J.-P. Uzan, M. Yasuda, D.-H. Yu, C. Rieck, H. Schnatz, Y. Hanado, M. Fujieda, P.-E. Pottie, J. Hanssen, A. Malimon, and N. Ashby, "Roadmap towards the redefinition of the second," *Metrologia*, vol. 61, p. 012001, Feb. 2024.

[6] T. Schuldt, M. Gohlke, M. Oswald, J. Wüst, T. Blomberg, K. Döringshoff, A. Bawamia, A. Wicht, M. Lezius, K. Voss, M. Krutzik, S. Herrmann, E. Kovalchuk, A. Peters, and C. Braxmaier, "Optical clock technologies for global navigation satellite systems," *GPS Solutions*, vol. 25, p. 83, July 2021.

[7] "Atomic Time for a Networked World," *NIST*, June 2025. Last Modified: 2025-07-02T08:46-04:00.

[8] S. Kolkowitz, I. Pikovski, N. Langellier, M. Lukin, R. Walsworth, and J. Ye, "Gravitational wave detection with optical lattice atomic clocks," *Physical Review D*, vol. 94, p. 124043, Dec. 2016.

[9] D. Hanneke, B. Kuzhan, and A. Lunstad, "Optical clocks based on molecular vibrations as probes of variation of the proton-to-electron mass ratio," *Quantum Science and Technology*, vol. 6, p. 014005, Jan. 2021.

[10] F. Fama, "Waltz of the atoms: Collective behaviors in a [strontium] stream," Mar. 2025.

[11] T. Shi, D. Pan, and J. Chen, "Realization of phase locking in good-bad-cavity active optical clock," *Optics Express*, vol. 27, pp. 22040–22052, Aug. 2019.

[12] N. Skribanowitz, I. P. Herman, J. C. MacGillivray, and M. S. Feld, "Observation of Dicke Superradiance in Optically Pumped HF Gas," *Physical Review Letters*, vol. 30, pp. 309–312, Feb. 1973.

[13] J. G. Bohnet, Z. Chen, J. M. Weiner, D. Meiser, M. J. Holland, and J. K. Thompson, "A steady-state superradiant laser with less than one intracavity photon," *Nature*, vol. 484, pp. 78–81, Apr. 2012.

[14] D. Meiser, J. Ye, D. R. Carlson, and M. J. Holland, "Prospects for a Millihertz-Linewidth Laser," *Physical Review Letters*, vol. 102, p. 163601, Apr. 2009.

[15] J. Chen, "Active optical clock," *Science Bulletin*, 2009.

[16] M. A. Norcia, "Coupling atoms to cavities with narrow linewidth optical transitions: Applications to frequency metrology," *Journal of Physics B: Atomic, Molecular and Optical Physics*, vol. 52, p. 193001, Oct. 2019. arXiv:1908.11442 [physics].

[17] S. A. Schäffer, M. Tang, M. R. Henriksen, A. A. Jørgensen, B. T. R. Christensen, and J. W. Thomsen, “Lasing on a narrow transition in a cold thermal strontium ensemble,” *Physical Review A*, vol. 101, p. 013819, Jan. 2020.

[18] M. A. Norcia and J. K. Thompson, “Cold-Strontium Laser in the Superradiant Crossover Regime,” *Physical Review X*, vol. 6, p. 011025, Mar. 2016.

[19] T. Laske, H. Winter, and A. Hemmerich, “Pulse Delay Time Statistics in a Superradiant Laser with Calcium Atoms,” *Physical Review Letters*, vol. 123, p. 103601, Sept. 2019.

[20] H. Liu, S. B. Jäger, X. Yu, S. Touzard, A. Shankar, M. J. Holland, and T. L. Nicholson, “Rugged mHz-Linewidth Superradiant Laser Driven by a Hot Atomic Beam,” *Physical Review Letters*, vol. 125, p. 253602, Dec. 2020.

[21] A. Bisht, P. Arora, and V. G. Achanta, “Precision timekeeping with atomic clocks: evolution and future directions,” *Nature Communications*, vol. 17, p. 5284, June 2026.

[22] J. Levine, “Invited Review Article: The statistical modeling of atomic clocks and the design of time scales,” *Review of Scientific Instruments*, vol. 83, p. 021101, Feb. 2012.

[23] F. Riehle and John Wiley & Sons, eds., *Frequency standards: basics and applications*. Weinheim: Wiley-VCH, 2005. pg. 78.

[24] V. Gerginov, G. W. Hoth, T. P. Heavner, T. E. Parker, K. Gibble, and J. A. Sherman, “Accuracy evaluation of primary frequency standard NIST-F4,” *Metrologia*, vol. 62, p. 035002, Apr. 2025.

[25] J. Lodewyck, P. G. Westergaard, A. Lecallier, L. Lorini, and P. Lemonde, “Frequency stability of optical lattice clocks,” *New Journal of Physics*, vol. 12, p. 065026, June 2010.

[26] P. G. Westergaard, J. Lodewyck, L. Lorini, A. Lecallier, E. A. Burt, M. Zawada, J. Millo, and P. Lemonde, “Lattice-Induced Frequency Shifts in Sr Optical Lattice Clocks at the 10^{17} Level,” *Physical Review Letters*, vol. 106, p. 210801, May 2011.

[27] E. Oelker, R. B. Hutson, C. J. Kennedy, L. Sonderhouse, T. Bothwell, A. Goban, D. Kedar, C. Sanner, J. M. Robinson, G. E. Marti, D. G. Matei, T. Legero, M. Giunta, R. Holzwarth, F. Riehle, U. Sterr, and J. Ye, "Demonstration of 4.8×10^{17} stability at 1 s for two independent optical clocks," *Nature Photonics*, vol. 13, pp. 714–719, Oct. 2019.

[28] A. Quessada, R. P. Kovacich, I. Courtillot, A. Clairon, G. Santarelli, and P. Lemonde, "The Dick effect for an optical frequency standard," *Journal of Optics B: Quantum and Semiclassical Optics*, vol. 5, p. S150, Apr. 2003.

[29] J. Zhang, T. Shi, J. Miao, and J. Chen, "The development of active optical clock," *AAPPS Bulletin*, vol. 33, p. 10, Apr. 2023.

[30] J. P. Bartolotta, M. A. Norcia, J. R. K. Cline, J. K. Thompson, and M. J. Holland, "Laser cooling by sawtooth-wave adiabatic passage," *Physical Review A*, vol. 98, p. 023404, Aug. 2018.

[31] B. Laburthe-Tolra, Z. Amodjee, B. Pasquiou, and M. Robert-de Saint-Vincent, "Correlations and linewidth of the atomic beam continuous superradiant laser," *SciPost Physics Core*, vol. 6, p. 015, Mar. 2023.

[32] B. Laburthe-Tolra, M. Robert-de Saint-Vincent, and B. Pasquiou, "Instabilities of the continuous superradiant laser," June 2026. arXiv:2606.21675 [quant-ph].

[33] V. M. Schäfer, Z. Niu, J. R. K. Cline, D. J. Young, E. Y. Song, H. Ritsch, and J. K. Thompson, "Continuous momentum state lasing and cavity frequency-pinning with laser-cooled strontium atoms," May 2024. arXiv:2405.20952 [quant-ph].

[34] "Chapter 10. Statistical Optics," in *Fundamentals of photonics* (B. E. A. Saleh and M. C. Teich, eds.), Wiley series in pure and applied optics, Hoboken, NJ: Wiley-Interscience, 2001.

[35] M. D. Eisaman, J. Fan, A. Migdall, and S. V. Polyakov, "Invited Review Article: Single-photon sources and detectors," *Review of Scientific Instruments*, vol. 82, p. 071101, July 2011.

[36] R. J. Glauber, "The Quantum Theory of Optical Coherence," *Physical Review*, vol. 130, pp. 2529–2539, June 1963.

[37] "Chapter 4. Field-field and photon-photon interferometry," in *Quantum optics*, Cambridge New York Melbourne Madrid Cape Town Singapore Sao Paulo Delhi Dubai Tokyo Mexic City: Cambridge University Press, 2008.

[38] C. Gerry and P. Knight, "Introductory Quantum Optics,"

[39] Ajbura, "Photon detections as a function of time."

[40] Jason Ball, "Calculating g(2) using the Moku TFA."

[41] C.-H. Huang, Y.-H. Wen, and Y.-W. Liu, "Measuring the second order correlation function and the coherence time using random phase modulation," *Optics Express*, vol. 24, p. 4278, Feb. 2016.

[42] S. Reynaud, "La fluorescence de résonance : Etude par la méthode de l'atome habillé," *Annales de Physique*, vol. 8, pp. 315–370, 1983.

[43] R. Loudon, *The quantum theory of light*. Oxford science publications, Oxford ; New York: Oxford University Press, 3rd ed ed., 2000.

[44] J. W. Goodman, *Statistical optics*. Wiley series in pure and applied optics, Hoboken, New Jersey: John Wiley & Sons Inc, second edition ed., 2015.

[45] J. Andreasen, H. Cao, A. Taflove, P. Kumar, and C.-q. Cao, "Finite-difference time-domain simulation of thermal noise in open cavities," *Physical Review A*, vol. 77, p. 023810, Feb. 2008.

[46] "Chapter 1. Fundamentals of radiative transfer," in *Radiative processes in astrophysics*, Weinheim, [Germany]: Wiley-VCH Verlag GmbH & Co. KGaA, 2004.

[47] A. Donges, "The coherence length of black-body radiation," *European Journal of Physics*, vol. 19, p. 245, May 1998.

[48] C. L. Mehta, "Coherence-time and effective bandwidth of blackbody radiation," *Il Nuovo Cimento (1955-1965)*, vol. 28, pp. 401–408, Apr. 1963.

[49] R. H. Brown and R. Q. Twiss, "Correlation between Photons in two Coherent Beams of Light," *Nature*, vol. 177, pp. 27–29, Jan. 1956.

[50] A. Gulinatti, "Single photon avalanches diodes," *Photoniques*, no. 125, pp. 63–68, 2024.

[51] G. Ferioli, S. Pancaldi, A. Glicenstein, D. Clément, A. Browaeys, and I. Ferrier-Barbut, "Retraction: Non-Gaussian Correlations in the Steady State of Driven-Dissipative Clouds of Two-Level Atoms [Phys. Rev. Lett. 132, 133601 (2024)]," *Physical Review Letters*, vol. 136, p. 149902, Apr. 2026.

[52] G. A. Steudle, S. Schietinger, D. Höckel, S. N. Dorenbos, I. E. Zadeh, V. Zwiller, and O. Benson, "Measuring the quantum nature of light with a single source and a single detector," *Physical Review A*, vol. 86, p. 053814, Nov. 2012.

[53] M. Assmann and M. Bayer, "Coherence time measurements using a single detector with variable time resolution," *Optics Letters*, vol. 37, p. 2811, July 2012.

[54] W. Martienssen and E. Spiller, "Coherence and Fluctuations in Light Beams," *American Journal of Physics*, vol. 32, pp. 919–926, Dec. 1964.

[55] T. A. Kuusela, "Measurement of the second-order coherence of pseudothermal light," *American Journal of Physics*, 2017.

[56] "MIT Spectroscopy Lab - History."

[57] R. Paschotta, "Wavemeters - an encyclopedia article," in *RP Photonics Encyclopedia*, RP Photonics AG, 2007.

[58] R. Paschotta, "Beat Note - an encyclopedia article," in *RP Photonics Encyclopedia*, RP Photonics AG, 2005.

[59] A. Javan, W. R. Bennett, and D. R. Herriott, "Population Inversion and Continuous Optical Maser Oscillation in a Gas Discharge Containing a He-Ne Mixture," *Physical Review Letters*, vol. 6, pp. 106–110, Feb. 1961.

[60] T. W. Hänsch, "Nobel Lecture: Passion for precision," *Reviews of Modern Physics*, vol. 78, pp. 1297–1309, Nov. 2006.

[61] J.-Q. Chen, C. Chen, J.-J. Sun, J.-W. Zhang, Z.-H. Liu, L. Qin, Y.-Q. Ning, and L.-J. Wang, "Linewidth Measurement of a Narrow-Linewidth Laser: Principles, Methods, and Systems," *Sensors*, vol. 24, p. 3656, June 2024.

[62] G. Di Domenico, "Laser Lineshape and Frequency Fluctuations | Wolfram Demonstrations Project," 2011.

[63] S. V. Kashanian, A. Eloy, W. Guerin, M. Lintz, M. Fouché, and R. Kaiser, "Noise spectroscopy with large clouds of cold atoms," *Physical Review A*, vol. 94, p. 043622, Oct. 2016.

[64] D. R. Paschotta, "Optical Heterodyne Detection," *RP Photonics Encyclopedia*, Oct. 2009.